 Bull. Chem. Soc. Jpn. Vol. 82, No. 2, 127–151 (2009)

Award Accounts

The Chemical Society of Japan Award for Creative Work for 2007

Study on the Structure and Vibrational Dynamics of Functional Molecules and Molecular Clusters by Double Resonance Vibrational Spectroscopy

Takayuki Ebata

Department of Chemistry, Graduate School of Science, Hiroshima University, Higashi-Hiroshima 739-8526

Received August 20, 2008; E-mail: tebata@hiroshima-u.ac.jp

Structure and dynamics of gas-phase molecules and their clusters formed in a supersonic jet has been a great interest to many researchers. Studies on these simple systems provide us with the fundamental concept of many physical and chemical phenomena observed in bulk systems. These studies are also important for the verification of theoretical prediction and quantum chemical calculations. Especially molecular clusters have been thought to be a good model for molecular level understanding of intermolecular interaction and relaxation in condensed phase. However, until the beginning of 1990, studies of molecular clusters mainly concentrated on electronic spectroscopy and very few studies were reported for vibrational spectroscopy. On the other hand, vibrational spectroscopy is essential in condensed phase, and there has been a gap between cluster science and condensed phase science. In 1993 we first reported infrared (IR)–ultraviolet (UV) double resonance spectroscopy of the OH stretching vibration of phenol and its hydrated clusters in a supersonic jet. The observed vibrational spectra showed a characteristic feature of the H-bonding, that is a larger frequency shift as well as broadening of the OH stretching band, and the structures were unambiguously determined with the aid of quantum chemical calculation. It is not too much to say that the combination of double resonance vibrational spectroscopy and quantum chemical calculation has become a very popular method in cluster science. In this paper, we describe various double resonance vibrational spectroscopies in frequency domain. Typical examples of application are shown; determination of H-bonded clusters of benzonitrile, conformer selective vibrational spectroscopy for L-phenylalanine and its hydrated cluster, and study of the encapsulation structure of guest atom and molecules by functional molecules, calixarene and crown ether. Finally, time-domain studies for the dynamics of the vibrations are described. Picosecond IR–UV pump–probe spectroscopy is applied to study the vibrational energy relaxation (VER) of the OH stretching vibration of isolated aromatic molecules and the H-bonded clusters.

1. Introduction

Clusters in which a molecule is surrounded by other molecules have been thought to be a molecular-level model for solute–solvent systems, providing a medium for the microscopic investigation of the properties of condense phase. Extensive development of supersonic molecular beam technique and laser-based spectroscopic methods allow us to study the structure and dynamics of size-selected molecular clusters. Though there still exists a large gap in properties between clusters and condensed phases, we expect that collective chemical properties in solutions can be interpreted in terms of local structures and dynamics of the intermolecular surrounding, that is the molecular cluster.

The intermolecular structures as well as dynamic behavior of clusters have been studied mostly by spectroscopic methods both in frequency and time domain. Among several spectroscopic methods, vibrational spectroscopy has made great progress over the past ten years in characterizing the structure of size-selected neutral as well as ionic molecular clusters. The importance of using vibrational spectroscopy is that most studies in condensed phase are based on vibrational spectroscopy, either in frequency or time domain, and it is necessary to provide information of the vibration of clusters for direct comparison with those of condensed phase studies. In this report, we will concentrate our interest on the vibrational spectroscopy of neutral clusters. Different from ionic clusters, mass spectrometric methods are not effective for size-selection so vibrational spectroscopic study of neutral species has appeared much later than those of ionic clusters. Huisken and co-workers[1] first reported an IR photodissociation spectroscopic study of small-size water clusters by using a novel size-selection technique involving molecular beam scattering which was developed by Buck and Meyer.[2] Direct high-resolution IR absorption spectroscopic measurement for water clusters has been extensively studied by Saykally's group.[3] Another powerful method for obtaining the vibrational spectra of neutral clusters is the double resonance method. The vibrational

Published on the web February 13, 2009; doi:10.1246/bcsj.82.127

excitation is carried out either by intense tunable IR laser light or stimulated Raman pumping and the population change induced by the vibrational excitation is monitored by the electronic transition. Either laser-induced fluorescence (LIF) or resonance-enhanced multiphoton ionization (REMPI) is used, which works as size- and isomer-selection as well as extremely sensitive detection. Double resonance between the IR laser excitation and UV laser probe, called IR–UV double resonance spectroscopy, was first reported by Brutschy and co-workers for the observation of CO stretching vibration,[4] where they used CO laser for vibrational excitation. Lee and co-workers used optical parametric oscillation (OPO) as a tunable IR laser light source and measured IR spectra of the CH stretching vibration of benzene and benzene dimer.[5] Double resonance between stimulated Raman pumping and a UV laser probe, called stimulated Raman–UV double resonance spectroscopy, was first applied by Owyoung and co-workers for gas-phase NO and benzene,[6] and Felker and co-workers extended this spectroscopy to clusters containing aromatic molecules.[7]

The most effective application of double resonance vibrational spectroscopy may be the measurement of the X–H stretching vibration (X refers to O, N, etc.) of hydrogen (H)-bonding clusters. It is well known that the X–H stretching vibration drastically changes band intensity and width upon H-bonding in condensed phase. To date, extensive studies have been carried out for understanding the local structure as well as dynamics of the X–H stretching vibration of H-bonded systems. In this sense, IR spectroscopic study of H-bonded clusters provides us with useful microscopic information on the H-bonding network of condensed phases. The first study by IR–UV double resonance spectroscopy of H-bonded clusters was reported by Mikami, Ebata, and co-workers for phenol–$(H_2O)_n$ clusters.[8] Almost at the same time, Zwier and co-workers carried out IR–UV double resonance spectroscopy measurements of benzene–$(H_2O)_n$ clusters.[9] The importance of these studies is that it has been demonstrated that the characteristic IR spectra of those systems are of substantial use for theoretical analyses based on quantum chemical calculations,[10] so that we can visualize the intermolecular structures. It is no exaggeration to say that double resonance vibrational spectroscopy is an indispensible tool for cluster science.[11]

The three-dimensional structures of peptides and proteins and their dynamics are to a large extent governed by the conformational profiles of amino acids constituting them. In particular, competition between intra- and intermolecular hydrogen-bonding interactions plays a vital role in determining the structure of these proteins in solution. Since amino acids exist as zwitterions in solution, it is interesting to investigate their hydrated structures. Such problems of conformation and zwitterionic formation can also be investigated by double resonance vibrational spectroscopy in supersonic jets.[12–21]

Another important aspect of the use of molecular clusters for condensed phase studies is to reveal the dynamics of vibrationally excited molecules and clusters. The vibrational energy relaxation (VER) has been the central issue in most of the chemical reactions in the condensed phase[22–33] as well as in the gas phase.[34–48] Among many vibrations investigated, the VER of the OH stretching vibration may be most important from the view point of elucidating the dynamics of the H-bonding of protic solvent molecules, such as water and alcohols, as well as the H-bonding of biologically relevant molecules.[49–54] The effect of H-bonding is easily seen in the vibrational spectrum of the OH stretching vibration in condensed phase; a large lower frequency shift, enhanced IR activity, and drastic broadening.[55] Picosecond IR–UV pump–probe spectroscopy is one of the most powerful tools for investigating the real-time VER of gas-phase molecules and clusters.[38,56–60] By observing VER in real time for clusters that are experimentally and theoretically well characterized, we can perform molecular level study of the dynamics of VER of the OH stretching vibration of molecules and H-bonded clusters.

Laser spectroscopic study of jet-cooled functional molecules is a newly started project in cluster science.[61,62] Functional molecules exhibit self assembly and work as a host for encapsulation of guest molecule(s).[63–66] As can be seen in previous studies, the encapsulation is fairly controlled by the conformation of host molecules and the non-covalent interaction between host and guest molecules. To date, most of the spectroscopic studies for host–guest complexes have been carried out at room temperature by absorption, fluorescence, NMR, IR, and Raman spectroscopy.[67–75] In the gas phase, mass spectroscopy has been used for the characterization of charged species.[76,77] On the other hand, the energy of the non-covalent interaction in complexes is comparable to the thermal energy so that we obtain only the averaged aspects of the host–guest complexes in bulk conditions. In this sense, cooling of the internal temperature of the complexes by the use of the supersonic jet and the combination with laser spectroscopy is promising to reveal the intrinsic nature of the non-covalent interaction leading to molecular recognition.

This paper is constructed as follows. We first describe the excitation schemes for several examples of double resonance vibrational spectroscopy and energy level diagrams of the molecular systems. We then demonstrate several examples of an application of double resonance vibrational spectroscopy. The first example is benzonitrile and its H-bonded clusters.[78–81] Here, we see that both the IR and Raman spectra exhibit important features characteristic of the structure. Second, we discuss the discrimination of conformations of amino acid, L-phenylalanine (L-Phe) and conformation specific hydration.[19,20] Third, we show our recent laser spectroscopic study of jet-cooled functional molecules, that is calixarene and crown ether. We report the structure of calix[4]arene–X_n ($X = Ar$ and Ne)[61] and hydrated clusters of dibenzo-18-crown-6-ether (DB18C6),[62] by using double resonance spectroscopy.

Finally, a time-resolved study of the vibrational energy relaxation (VER) of the OH stretching vibration, that is intramolecular and -cluster vibrational energy redistribution (IVR) and vibrational predissociation (VP) initiated by the IR excitation, of aromatic molecules and their clusters are described.[56–60] Here, picosecond time-resolved IR–UV pump–probe spectroscopic technique is used. We choose phenol and its isotope-substituted species. We show that in bare phenol, the OH vibrational energy is redistributed by two-steps, that is "initial level" → "doorway states" → "dense bath states," based on the analysis of the transient UV spectrum and its time evolution. We then describe the VER of the H-bonded clusters of phenol. From the analysis of the transient UV

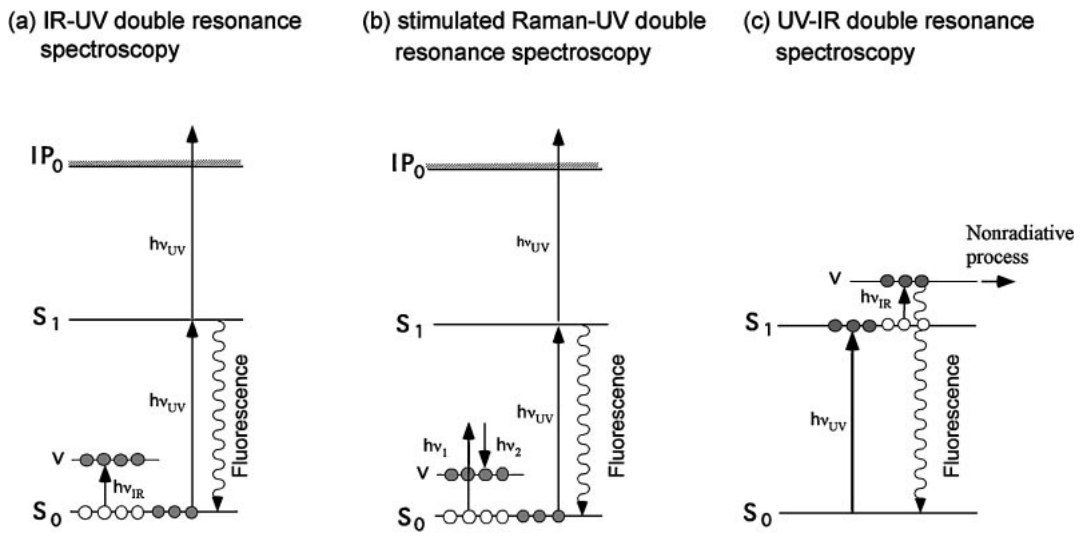

Figure 1. Energy level diagram and excitation schemes of double resonance vibrational spectroscopy for the ground and excited states of neutral molecules. (a) IR–UV double resonance spectroscopy, (b) stimulated Raman–UV double resonance spectroscopy, and (c) UV–IR double resonance spectroscopy.

spectra, we discuss the energy dissipation mechanism from the excited OH stretch to the dissociation of the H-bond.

2. Excitation Scheme and Experimental Setup for Frequency Domain Experiments

2.1 IR–UV and Stimulated Raman–UV Double Resonance Spectroscopy. Figures 1a and 1b shows excitation schemes of IR–UV and stimulated Raman–UV double resonance spectroscopy for the species in the ground electronic state (S_0). The lasers used in these experiments are pulsed nanosecond laser systems. In Figures 1a and 1b, jet-cooled molecules or clusters are pumped to a specific vibrational level by tunable IR laser (ν_{IR}) or by stimulated Raman excitation with ν_1 and ν_2. The depletion of the $v = 0$ level population induced by the vibrational excitation is monitored by the electronic transition with the UV laser (ν_{UV}). The delay time between the laser(s) for the vibrational excitation and the probe UV laser is normally set to 50–100 ns. The UV laser frequency is tuned to the vibronic band, usually the 0,0 band, of the species with different cluster size or conformation, and either fluorescence or REMPI signal is monitored. Thus, a fluorescence-dip or ion-dip vibrational spectrum is obtained by scanning the tunable IR frequency ($h\nu_{IR}$) or the difference frequency ($h(\nu_1 - \nu_2)$) while monitoring either the fluorescence or REMPI signal.

2.2 UV–IR Double Resonance Spectroscopy. Figure 1c shows the scheme of UV–IR double resonance spectroscopy for measuring the vibrational spectrum of the electronic excited species (S_1). The same laser system is used with that of IR–UV double resonance spectroscopy though the delay time between the IR and UV laser pulses is reversed. The UV laser first pumps the molecule to the zero-point level of S_1 and the fluorescence signal is monitored. The IR laser pulse, which is introduced at a delay time of several nanoseconds, excites the S_1 state molecule further to the upper vibrational level. Since the fluorescence quantum yield decreases at higher vibronic levels in most of aromatic molecules, a depletion is observed in the fluorescence signal when the molecule is pumped to the vibronic levels. Thus, a fluorescence-dip spectrum is obtained by scanning the tunable IR frequency ($h\nu_{IR}$) while monitoring the fluorescence signal.

2.3 Description of Laser System, Supersonic Jet, and Theoretical Calculation. Figure 2a shows the typical experimental setup of IR–UV double resonance vibrational spectroscopy. The clusters are generated by a supersonic expansion of a gaseous mixture of solute/solvent diluted with He. The mixture is expanded into vacuum through a pulsed nozzle having a 1 mm orifice. For vaporizing nonvolatile molecules such as amino acids, calixarene, and crown ethers, we developed a compact high-temperature pulsed nozzle, which is shown in Figure 2b. In this nozzle, a sample housing made of polyimide resin (DuPont Co., Vespel) is attached to the head of a commercially available pulsed nozzle (General valve series 9). The sample powder in the housing is heated at ≈200 °C by a spiral heater attached outside the housing. A poppet with a diameter of 1.7 mm and a length of 18 mm is driven by an electromagnet to expand the mixture of vaporized sample and carrier gas into vacuum. The poppet is also made of polyimide resin so that the nozzle is completely free from the metal. The valve (metal part) is also heated by another heater to prevent a temperature gradient inside the wall of the housing. The metal-free condition inside the housing is important to minimize thermal decomposition, which is a severe problem in vaporizing amino acids in a normal metal nozzle.

The IR and UV laser beams are collinearly focused into a vacuum chamber in a counterpropagated geometry. The tunable IR laser light is generated by difference frequency generation between the second harmonic of a nanosecond Nd^{3+}:YAG laser (Continuum powerlite 8010) and a Nd^{3+}:YAG laser pumped dye laser (Continuum ND 6000) with use of a $LiNbO_3$ crystal or an optical parametric oscillator/amplifier (OPO) laser system (Laser vision) pumped by the Nd^{3+}:YAG laser. For the stimulated Raman pumping, the second harmonics (532 nm) of Nd^{3+}:YAG laser is split into two by a beam splitter. One is

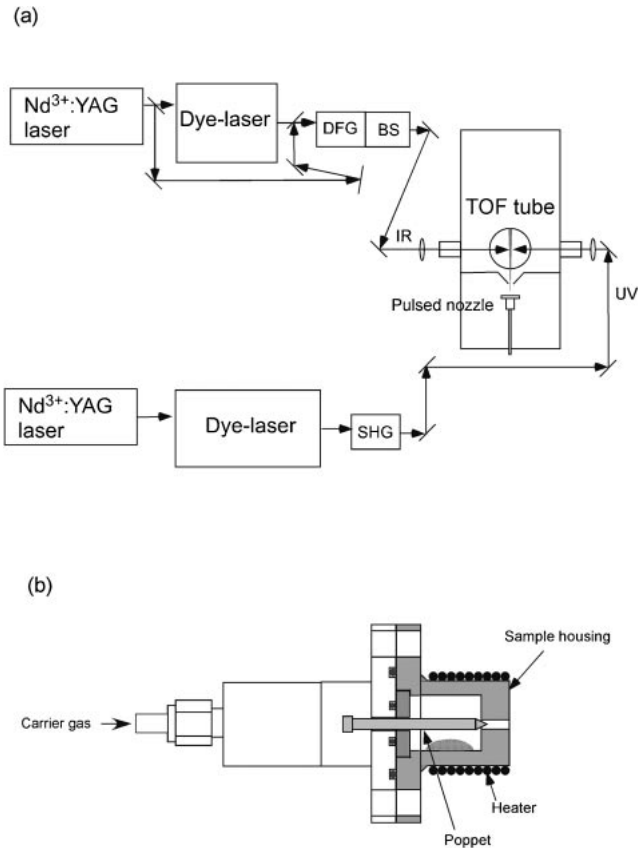

Figure 2. (a) Schematic view of the experimental setup of IR–UV double resonance spectroscopy. (b) Design of the high-temperature pulsed nozzle for obtaining the pulsed jet of nonvolatile molecules.

used for ν_1, and the other is used to pump a dye laser for obtaining ν_2. ν_1 and ν_2 are combined by a beam combiner and are introduced into a vacuum chamber. The UV laser light is a second harmonic of another Nd^{3+}:YAG laser pumped dye laser (Continuum Surelite-II/Lambda Physik scan mate). For the LIF measurement, the UV laser pulse crosses the jet at 30 mm downstream of the nozzle and the wavelength of the UV laser is scanned through the band origin of the S_1–S_0 transition. The fluorescence of the sample is collected by a series of lenses and detected by a photomultiplier tube (Hamamatsu Photonics 1P28). For mass-resolved REMPI measurement, a time-of-flight (TOF) mass-spectrometer is placed instead of the fluorescence collection optics. The supersonic jet is skimmed by a skimmer having a 2-mm aperture, and the molecules in a supersonic beam are ionized by $1 + 1$ REMPI with a tunable UV laser. The ions are repelled and extracted into the 50-cm length TOF tube. The ions are detected by a Channeltron (Burle 4900), amplified by a preamplifier, and monitored with a digital oscilloscope. Photocurrent and ion current are averaged with a boxcar integrator (Stanford research systems SR245) and processed by a personal computer.

Parallel to the experimental observation, the structures of the clusters are investigated by quantum chemical calculation at HF/6-31+G**, B3LYP/6-31+G*, or MP2/6-31+G* level with Gaussian 98 and 03 program package.[82] Though the calculation level of HF/6-31+G** is rather low at present, this level of calculation is still good enough to describe the hydrogen-bonding system where the electrostatic potential is important.

3. Application of Double Resonance Spectroscopy

3.1 H-Bonded Clusters of Benzonitrile. Benzonitrile (BN) has a large dipole moment (4.18 Debye) as well as a large polarizability (12.5 Å^3),[83] and it has three proton accepting sites for the hydrogen bond (H-bond), that is, (1) the triple bond of the CN group, (2) N atom of the CN group having nonbonding electrons, and (3) the π-electrons of the phenyl ring. This molecule is known to form clusters with various solvent molecules in supersonic jets, such as BN–$(H_2O)_n$, –$(CH_3OH)_n$, –$(CH_3CN)_n$, and –$(CF_3H)_n$.[84–87] Among them, clusters containing water or methanol have been paid much attention, since their structures result from a subtle balance of intermolecular forces involving electrostatic interactions and the H-bond. Here, we investigate the structures of BN–$(H_2O)_n$ and –$(CH_3OH)_n$ by examining three vibrational modes, that is OH(ν_{OH}), CN(ν_{CN}), CC(ν_{12}), and CH(ν_{CH}) stretching vibrations with double resonance vibrational spectroscopy, and by quantum chemical calculation.

3.1.1 Electronic Spectra of Benzonitrile and Its Clusters: Figure 3 shows the S_1–S_0 LIF spectra of bare BN, $(BN)_2$ (D), BN–$(H_2O)_{n=1-3}$, and BN–$(CH_3OH)_{n=1-3}$.[78] The band origin of bare BN is located at 36514.0 cm^{-1} and those of the clusters are red-shifted from the monomer band. For BN–$(H_2O)_{n=1-3}$, their assignments have been given by Kobayashi and Kajimoto from the dependence of the peak intensities on the concentration of water vapor.[85] Similar assignments can be given for BN–$(CH_3OH)_{n=1-3}$ from the similarity of the red-shifts of the band origins. Though electronic spectroscopy is useful to discuss the size of clusters, it sometimes misleads the determination of the structures. Actually, Kobayashi and Kajimoto suggested that in the $n = 2$ clusters, two H_2O molecules or CH_3OH molecules are located in symmetric positions with each other.[86] However, as we will discuss later, the combination of double resonance vibrational spectroscopy and quantum chemical calculation reveals a structure different from that predicted by electronic spectroscopy.

3.1.2 Vibrational Spectra of the Clusters of Benzonitrile: In this section, we examine the vibrational spectra for four vibrational modes of benzonitrile and its hydrogen-bonded clusters by double resonance vibrational spectroscopy. Each mode exhibits characteristic spectral shift upon H-bonding, which are very well correlated with the binding site.

3.1.2.1 OH Stretching Vibrations (ν_{OH}); The OH stretching vibration (ν_{OH}) is the most important mode for the investigation of the structure of H-bonded clusters. The fluorescence-detected IR–UV double resonance spectra of ν_{OH} of BN–$(H_2O)_{n=1-3}$ and –$(CH_3OH)_{n=1-3}$ are shown in Figure 4. As seen in the figure, each spectrum exhibits $2n$ and $n\nu_{OH}$ bands for BN–$(H_2O)_{n=1-3}$ and –$(CH_3OH)_{n=1-3}$, respectively, which are equal to the number of OH oscillators of the H_2O and CH_3OH sites. In the IR spectra of BN–H_2O, two ν_{OH} bands are observed at 3614 and 3727 cm^{-1}. In BN–$(H_2O)_{n\geq 2}$, the vibrations can be classified into two groups; the vibrations showing remarkable red-shifts with the increase of n, and others appearing at $\approx$3720 cm^{-1}. The former group is assigned to the H-bonded

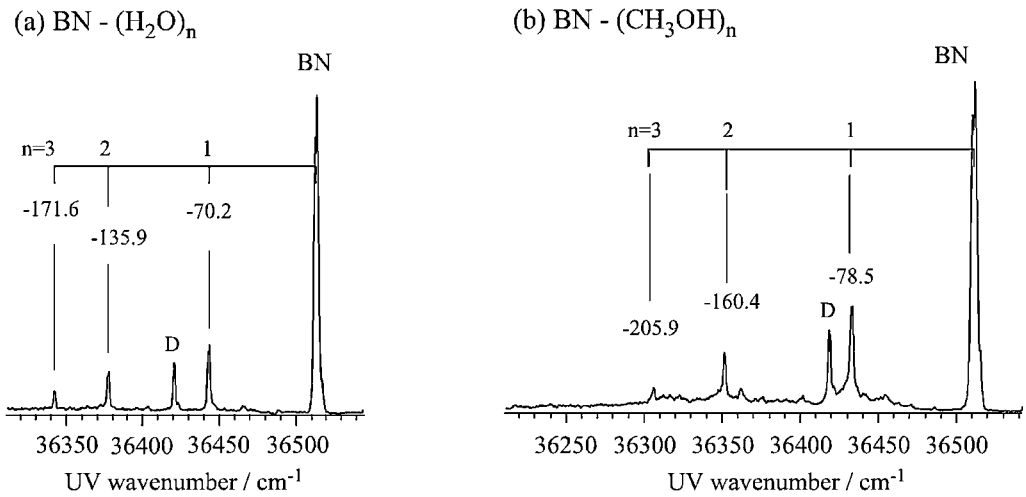

Figure 3. LIF spectra of benzonitrile (BN), BN dimer (D), BN–$(H_2O)_n$, and BN–$(CH_3OH)_n$ in supersonic jets.

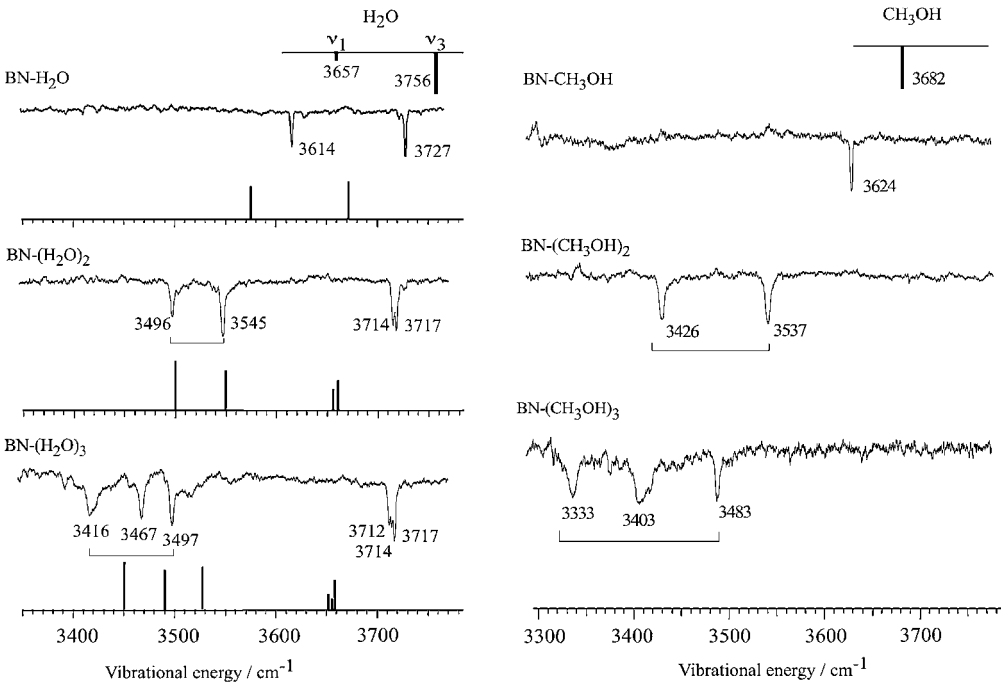

Figure 4. Fluorescence-detected IR–UV double resonance spectra of BN–$(H_2O)_n$ (left) and BN–$(CH_3OH)_n$ (right) in the region of the OH stretching vibration. Stick diagrams are the calculated IR spectra corresponding the structures of Figure 7. Figure adapted from Ref. 78.

ν_{OH} of H_2O and the latter to ν_{OH} free from the H-bond. Such a large frequency gap between the H-bonded ν_{OH} and the free ν_{OH} is a common feature for the clusters with a ring-form such as phenol–$(H_2O)_n$[8] and 2-naphthol–$(H_2O)_n$.[88] The H-bonded ν_{OH} bands of the IR spectra of BN–$(CH_3OH)_{n=1-3}$ exhibit a similar feature to those of BN–$(H_2O)_n$. The H-bonded ν_{OH} band of BN–CH_3OH appears at 3624 cm^{-1}. The H-bonded ν_{OH} bands split and shift to red with an increase of n. The spectral feature suggests a similar ring-form H-bonded network for these clusters.

3.1.2.2 CN Stretching Vibration (ν_{CN}); The fluorescence-detected stimulated Raman–UV double resonance spectra of BN, BN–$(H_2O)_{n=1-3}$, and BN–$(CH_3OH)_{n=1-3}$ in the ν_{CN} region are shown in Figure 5. Two bands were observed at 2244.1 and 2258.1 cm^{-1} in the spectrum of bare BN. The former intense band is assigned to ν_{CN}, and the latter band is assigned to the $\nu_1 + \nu_{19a}$ combination band with A_1 symmetry, which may appear by borrowing the intensity from the ν_{CN} fundamental. Both BN–$(H_2O)_{n=1-3}$ and –$(CH_3OH)_{n=1-3}$ exhibit anomalous frequency shifts for the ν_{CN} band. ν_{CN} of BN–H_2O and –CH_3OH is red-shifted with respect to bare BN. For the clusters with $n > 1$, in contrast, the ν_{CN} band shifts to blue and splits into two. The magnitude of the blue-shift of the ν_{CN} band of BN–$(H_2O)_3$ is as large as 12 cm^{-1} from that of the monomer. In addition to the anomalous shift, the ν_{CN} band splits into two for $n \geq 2$ of BN–$(H_2O)_n$ and for $n \geq 1$ of

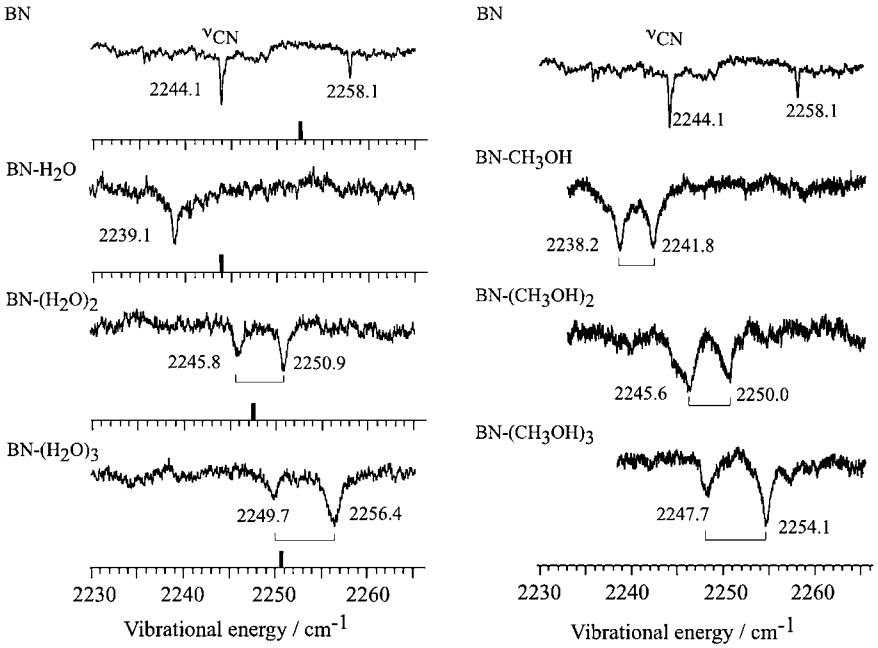

Figure 5. Fluorescence-detected stimulated Raman–UV double resonance spectra of BN–$(H_2O)_n$ (left) and BN–$(CH_3OH)_n$ (right) in the region of the CN stretching vibration. Figure adapted from Ref. 78.

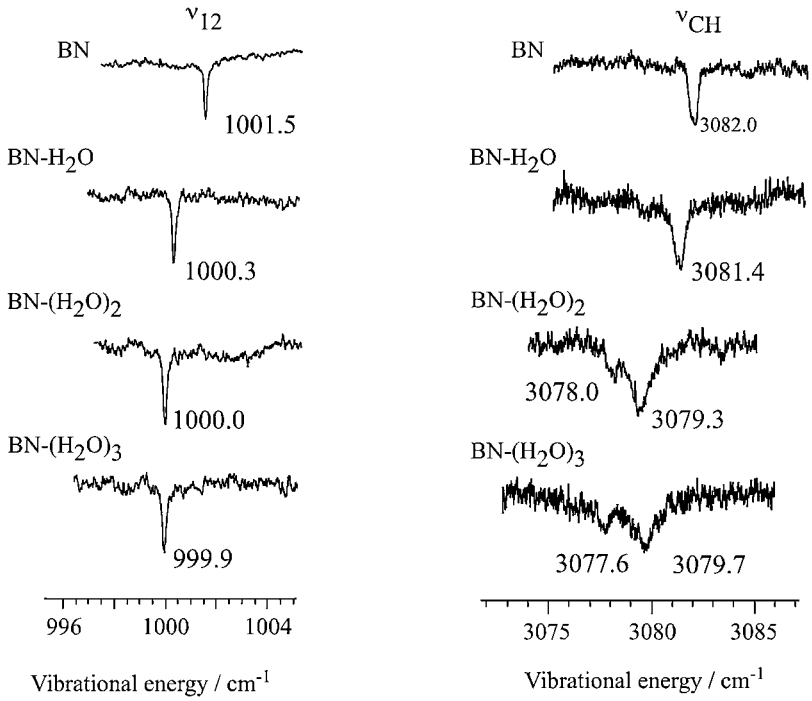

Figure 6. Fluorescence-detected stimulated Raman–UV double resonance spectra of BN–$(H_2O)_n$ in the CC stretch (ν_{12}) (left) and CH stretch (ν_{CH}) (right) vibrational regions. Figure adapted from Ref. 78.

$(CH_3OH)_n$. The splitting may be ascribed to Fermi resonance with the $\nu_1 + \nu_{19a}$ combination band which appeared at 2258.1 cm^{-1} in bare BN.

3.1.2.3 CC (ν_{12}) and CH (ν_{CH}) Stretching Vibrations; Figure 6 shows the fluorescence-detected stimulated Raman–UV double resonance spectra of CC (ν_{12}) and CH (ν_{CH}) stretching vibrations of BN–$(H_2O)_{n=1-3}$. In contrast to the substantial shifts of the ν_{CN} band, those of ν_{12} and ν_{CH} upon cluster formation are small. The ν_{12} band of BN–$(H_2O)_n$ exhibits a very sharp dip and the red-shift is less than 2 cm^{-1} even for BN–$(H_2O)_3$, representing that ν_{12} is almost unaffected by the H-bonding. The ν_{CH} band of bare BN is observed at 3082.0 cm^{-1}, and the red-shift is 3 cm^{-1} for BN–$(H_2O)_3$. In the $n = 2$ and 3 clusters, a satellite band is observed at the lower frequency side of ν_{CH}. This satellite band may be assigned to either a combination band or an overtone band whose intensity is borrowed by Fermi resonance. Different from ν_{12}, the width of the ν_{CH} band becomes broad with the size of the cluster,

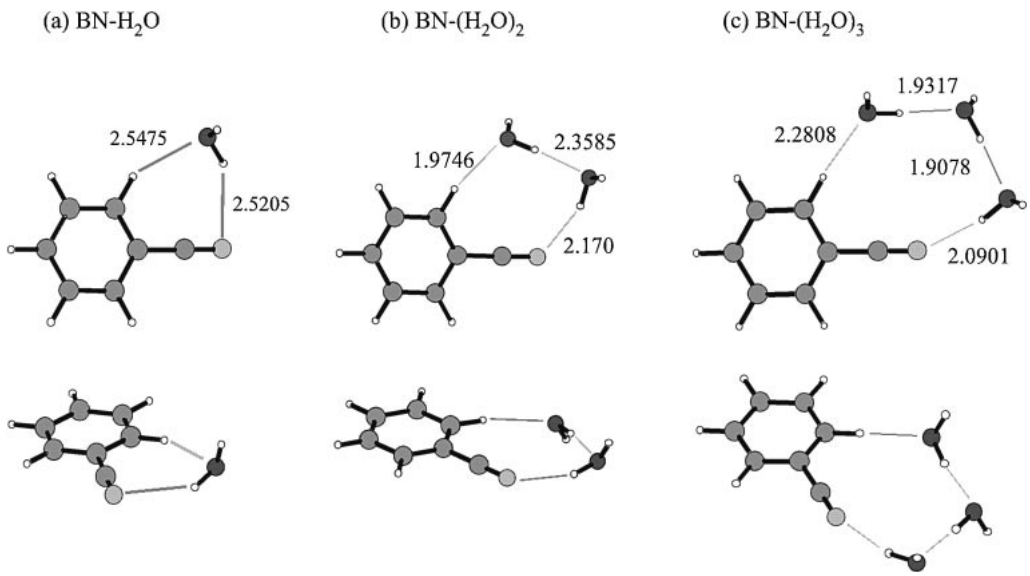

Figure 7. Most probable structures of BN–$(H_2O)_{n=1-3}$ optimized at HF/6-31G(d,p) level. The numbers are the H-bond distances in units of Å.

which can be described by the faster intracluster vibrational energy redistribution (IVR) of this mode.

3.1.3 Structure of Benzonitrile–$(H_2O)_n$ and –$(CH_3OH)_n$: Figure 7 shows the most probable structures of BN–$(H_2O)_{n=1-3}$ obtained by ab initio calculations at HF/6-31G** level. As was described in the experimental section, even this level of calculation well describes the H-bonding in which electrostatic interaction is dominant. Each structure is the most stable form in each size. The calculated IR spectra for the corresponding structures are shown in Figure 4 for ν_{OH}, and in Figure 4 for ν_{CN}, which show good agreement with the observed spectra. All the structures are ring-type as predicted from the experimental IR spectra of ν_{OH}. In BN–H_2O, the hydrogen of H_2O is bound to the N-end of the CN group and the oxygen forms a CH···O type H-bond to the *ortho*-CH of BN. The structure can be called "side-type" structure. This structure was predicted by Neusser and co-workers from high-resolution LIF measurement.[87] In the larger clusters ($n \geq 2$), water molecules tend to form a chain-form H-bonded cluster by themselves, such as dimers and trimers, and the chain-form cluster is bound to the N-end of the CN group and to the *ortho*-CH of BN. It is very interesting that with an increase of the size of water cluster the direction of the H-bonding of H_2O hydrogen with respect to the N-end of the CN group changes from side to linear. Such change is reflected in the complex shift of the ν_{CN} band. Though we did not carry out the calculation for BN–$(CH_3OH)_{n=1-3}$, similar structures with those of BN–$(H_2O)_{n=1-3}$ can be predicted from the observed spectra.

3.1.4 Low Frequency Raman Spectra: Raman spectra in the region lower than a few hundred cm^{-1} have been the subject of interest in condensed phase. The vibrations in this region are assigned to librational mode. Figure 8 shows the fluorescence-detected stimulated Raman–UV double resonance spectra of BN–$(H_2O)_{n=1-3}$ in the region below 50 cm^{-1}. In these measurements, an enhanced fluorescence signal due to stimulated Raman pumping is monitored. It should be noted that though the excitation scheme of this measurement is not described in the experimental section, we observe a broad hot band transition from the Raman pumped levels or relaxed levels in some systems after the stimulated Raman pumping. In BN–$(H_2O)_n$, we can observe the hot band transition in the lower frequency side of the 0,0 band of each cluster. Thus, by monitoring the hot band while scanning the Raman pumping laser frequency, we obtain the stimulated Raman spectrum for the cluster. In the spectrum, the band in the 0–4 cm^{-1} region is assigned to the rotational Raman band, which appears by the nonzero derivative of the polarizability with respect to the molecular rotation. In BN–$(H_2O)_{n=1-3}$, the peaks due to the intermolecular motion are seen at 31 cm^{-1} for $n = 1$, 27.3 and 39.5 cm^{-1} for $n = 2$, and 19.2, 27.3, and 30.3 cm^{-1} for $n = 3$, respectively. The frequency of the lowest frequency intermolecular band decreases with an increase of the cluster size. Figure 8 also shows the vector motion of the lowest frequency vibration of BN–$(H_2O)_{n=1-3}$ obtained by calculation at HF/6-31G** level and the calculated Raman spectra are shown as a stick diagram in the figure. As seen in the vector motions, the Raman active motion is the out-of-plane vibrational mode. This motion has a nonzero derivative of the polarizability with respect to the internal rotation of BN, similar to the rotational Raman band. Thus, it is common that the Raman active low frequency mode involves such an internal rotational motion in the cluster.

3.2 Discrimination of Conformation and a Conformation Specific Hydration of L-Phenylalanine. 3.2.1 Conformation Landscape of L-Phenylalanine: The conformational landscape of isolated L-phenylalanine (L-Phe) has been examined in detail.[19,20,89–91] In this section, we discuss the discrimination and the determination of the conformation of jet-cooled L-Phe by use of IR–UV double resonance spectroscopy with the aid of quantum chemical calculation. We also show that photophysics and the hydration structures are largely dependent on the conformation of L-Phe.

LIF and 1 + 1 REMPI spectra of jet-cooled L-Phe are shown in Figure 9a. There are several peaks in the band origin region,

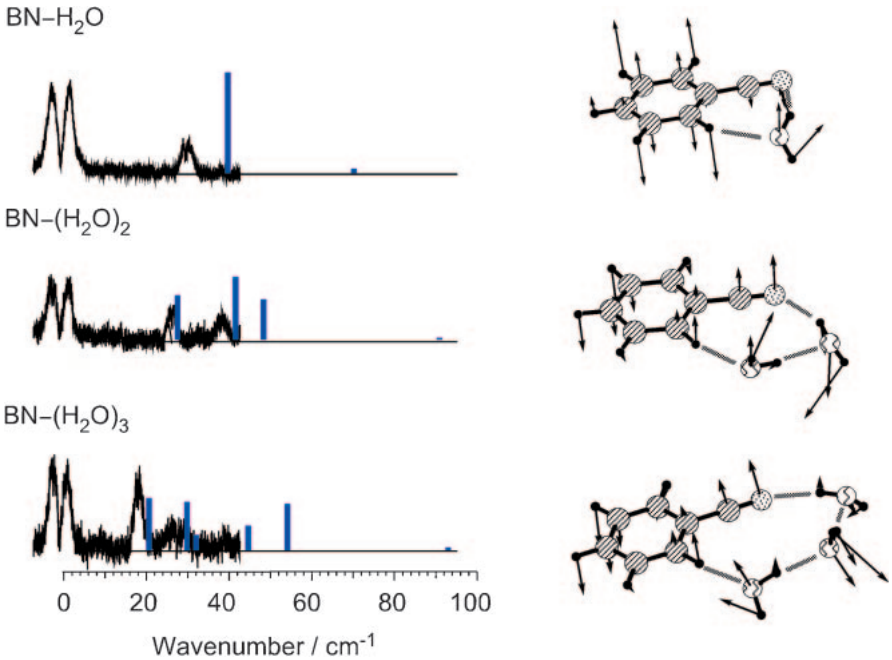

Figure 8. (left) Fluorescence-detected stimulated Raman–UV double resonance spectra of BN–$(H_2O)_{n=1-3}$ in the region of the intermolecular vibration. The spectra are shown as fluorescence gain spectra. Stick diagrams are the calculated Raman intensities. (right) Vector motions of the lowest frequency Raman active vibration of each cluster. Figure adapted from Ref. 81.

and Figure 9b shows the IR spectra by monitoring the marked bands (A, B, C, D, E, and X) in the LIF spectrum. Their IR spectra are different from each other, and it is concluded that there are at least six conformers of L-Phe in the jet. Other peaks have been assigned to the vibronic bands of each conformer by Simons and co-workers.[89] It is obvious that the relative band intensity in the LIF spectrum is quite different from that of the $1 + 1$ REMPI spectrum. From the fluorescence lifetime measurement, it was found that the fluorescence lifetime is different for different conformer. In particular, the lifetime of the species corresponding to band X is 29 ns, while those of other conformers are 70–90 ns.[19] Thus, the difference of the band intensity between LIF and $1 + 1$ REMPI spectra is mainly due to the difference of the fluorescence quantum yield. The short lifetime of conformer X, which has intramolecular H-bonding, may be ascribed to fast internal conversion or intersystem crossing to the nearby $n\pi^*$ state. Figure 10 shows the structures of conformers corresponding to the six species calculated at B3LYP/6-31+G* level. The number in the parentheses are the zero-point-energy corrected relative energy (kJ mol^{-1}) obtained at MP2/6-31+G* level. The species corresponding to bands X and B have an intramolecular H-bond between the carboxylic OH and N-atom of the amino group, so that H-bonded OH stretch of the carboxyl group is drastically red-shifted. The remaining four species (A, C, D, and E) have a non-H-bonded open-type form. Thus, six conformers are identified from the double resonance vibrational spectroscopic study and they have different fluorescence lifetimes.

3.2.2 Hydration of L-Phenylalanine: We then investigate the hydration structure of L-Phe. Figure 11 shows the LIF spectra of jet-cooled L-Phe measured under different partial pressure condition of water vapor in the He expansion. Here,

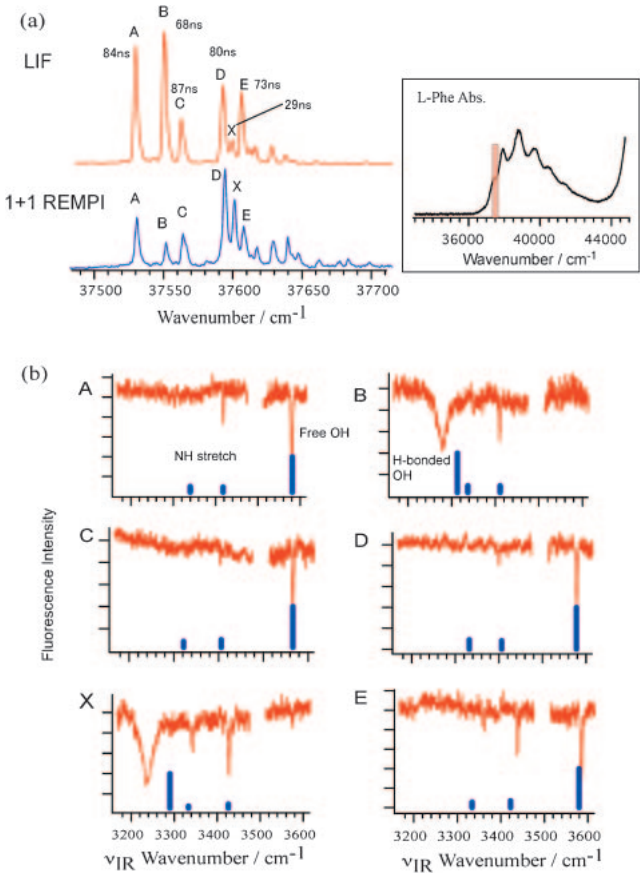

Figure 9. (a) LIF and $1 + 1$ REMPI spectra of jet-cooled L-Phe. (b) IR–UV double resonance spectra of L-Phe for the bands marked in the LIF spectrum. Stick diagrams are the calculated IR spectrum of the corresponding conformers shown in Figure 10.

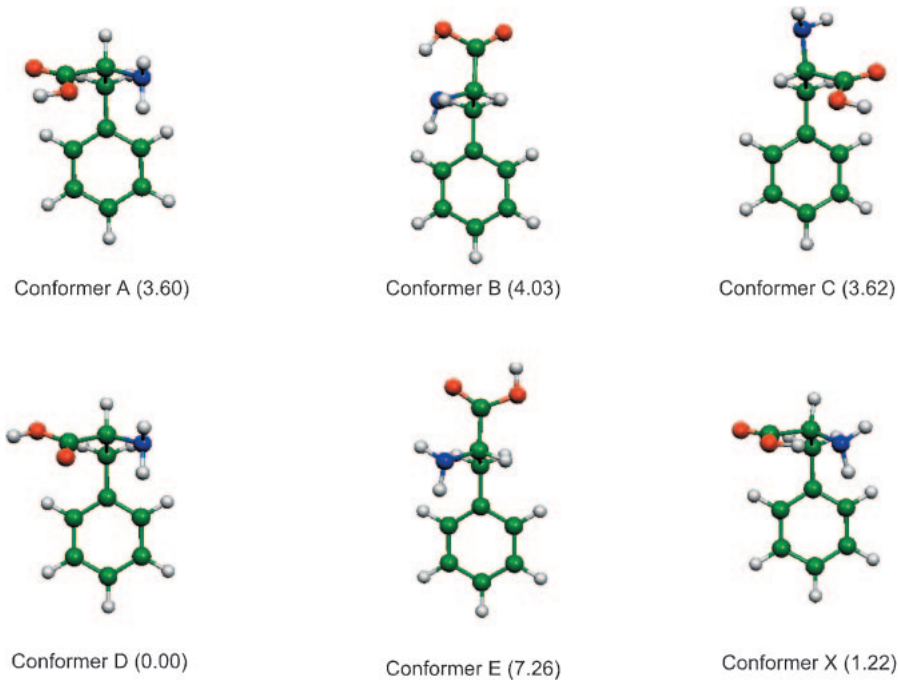

Figure 10. Optimized structures of L-Phe corresponding the bands marked in Figure 9a obtained at B3LYP/6-31+G* level. The numbers are the zero-point energy (ZPE) corrected relative energies calculated at MP2/6-31+G* level. See Ref. 20.

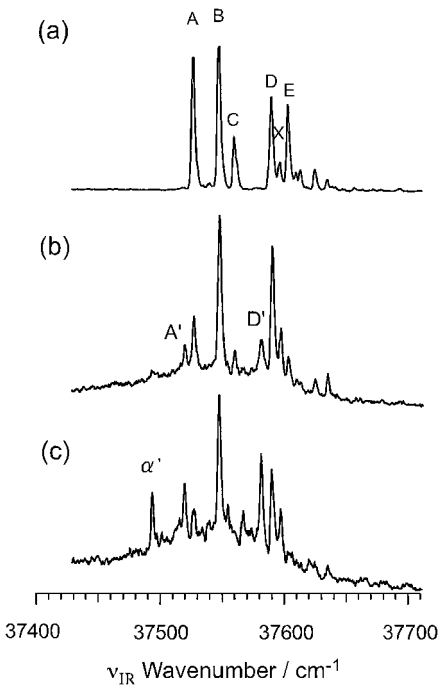

Figure 11. LIF spectrum of jet-cooled L-Phe at different partial pressure of water vapor; (a) without an addition of water vapor, (b) with an addition of small amount of water vapor, and (c) with a large amount of water vapor. Figure adapted from Ref. 20.

the partial pressure of water vapor increases in the order from (a) to (c). The spectra of Figures 11b and 11c are measured at higher sensitivity than that of Figure 11a, and normalized so that the intensity of band B is unity. As seen in Figure 11b, the band intensities due to conformers A, D, and E become much weaker than those of B, and bands A′ and D′ newly appear at 37520 and 37582 cm^{-1}, respectively. Thus, it is concluded that water molecules exclusively form H-bonding to the open-type conformers A, D, and E. This conformer-selective H-bond formation was suggested previously,[92] and is also found in other aromatic acids, such as 3-indole-propionic acid.[93] At higher partial pressure of water (Figure 11c), another band (band α') appears at 37494 cm^{-1}. This band was assigned to L-Phe–$(H_2O)_2$ by mass-selected $1 + 1'$ REMPI measurement by Kim and co-workers,[92] though the peak is observed only at the mass of $[L\text{-Phe}]^+$ and $[L\text{-Phe}–(H_2O)_1]^+$, due to the fragmentation after the ionization.

The IR spectra observed by fixing UV frequencies to bands A′, D′, and α' are shown in Figure 12. In the FDIR spectrum of band A′, which was assigned to L-Phe–$(H_2O)_1$,[92] there are two intense bands at 3246 and 3506 cm^{-1}, and three sharp bands at 3040, 3421, and 3724 cm^{-1}. Though it is a priori not clear whether L-Phe retains a similar conformation under the formation of the H-bonding with water, it is reasonable to assume that the isomer due to band A′ may have L-Phe conformation similar to conformer A of bare L-Phe, because the intensity of band A′ increases parallel to the decrease of band A, and the small red-shift in the electronic transition of band A′ with respect to band A (7 cm^{-1}) is also observed in other monohydrated aromatic acids.[93] Thus, we calculated the structures of L-Phe–$(H_2O)_1$ with L-Phe forming conformer A. In the calculation, we first considered three H-bonding sites; the carboxyl group, the amino group, and the phenyl group. We found that the H-bonding to the carboxyl group results in the most stable isomer, and the calculated IR spectrum reproduces very well the observed one.[20] Figure 12a also shows the most stable isomer (Aw1-I) and the calculated IR

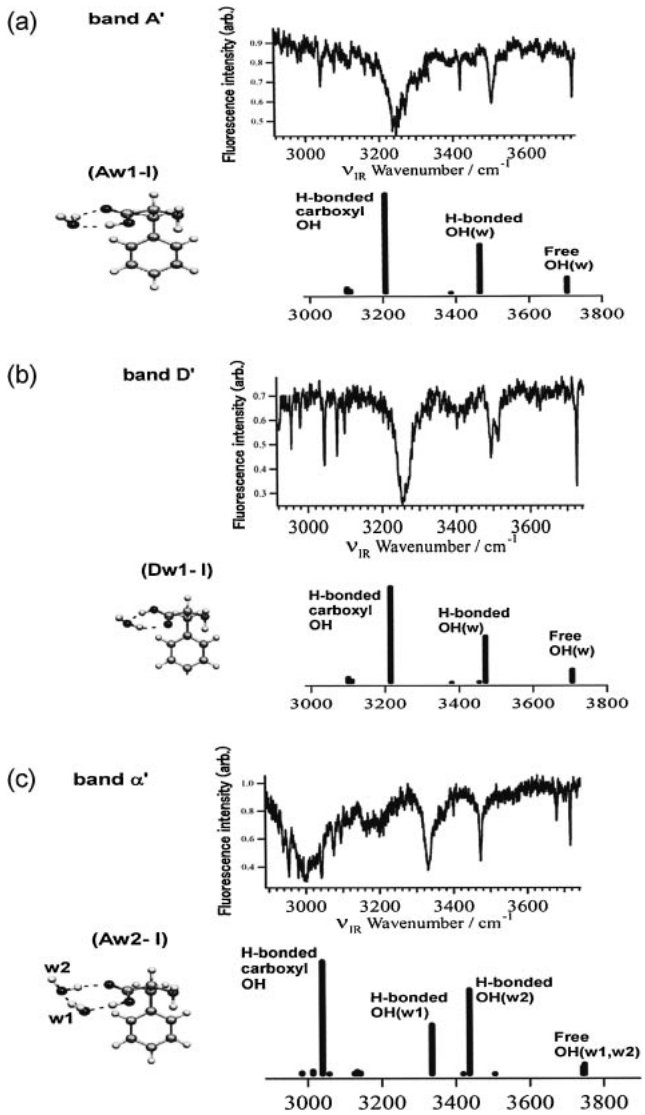

Figure 12. IR–UV double resonance spectra of L-Phe–$(H_2O)_{n=1,2}$ by monitoring the bands marked in Figure 9a. Stick diagrams are the calculated IR spectra and the corresponding structures obtained at B3LYP/6-31+G* level. Figure adapted from Ref. 20.

spectrum. In this isomer, the water forms a cyclic H-bond with the carboxyl group and this structure is assigned to band A′. The bands observed in the IR spectrum are assigned as follows; the intense and broad bands at 3246 and 3506 cm^{-1} are the H-bonded carboxyl OH and the water donor OH stretch bands, respectively, within the cyclic H-bonding network. The sharp bands at 3421 and 3724 cm^{-1} are assigned to the asymmetric NH_2 stretch of amino group and free OH stretch of water, respectively. The IR spectrum of band D′ (Figure 12b) is similar to that of band A′. Kim and co-workers suggested[92] that the isomer due to band D′ may have the same conformation as conformer D of bare L-Phe, because the red-shift of band D′ from band D in the electronic transition, that is 8.5 cm^{-1}, is close to that of band A′ from band A. Thus, we calculated the structure of L-Phe–$(H_2O)_1$ with L-Phe forming conformer D. It was found that similar to Aw1-I the isomer in which the water molecule forms a cyclic H-bond with the carboxyl group (Dw1-I) is the most stable structure and the spectrum of Dw1-I well reproduces the observed one.

Figure 12c shows the IR spectrum obtained by fixing UV frequency to band α′. In the spectrum, a very broad and strong band is seen at 3002 cm^{-1}. Several sharp bands are overlapped with this broad band, which are assigned to the aromatic CH stretch. Other intense peaks are seen at 3330, 3474, 3680, and 3717 cm^{-1}. The two bands at 3680 and 3717 cm^{-1} are easily assigned to the OH stretch of water molecules free from H-bonding, and the appearance of the two free OH stretch bands indicates the band α′ to be L-Phe–$(H_2O)_2$. Since band α′ is located at lower frequency than bands A and A′ in the LIF spectrum (Figure 11c), L-Phe in this cluster is thought to have a conformation similar to those of bands A (L-Phe) and A′ (L-Phe–$(H_2O)_1$). The calculated possible structures of L-Phe–$(H_2O)_2$ and their IR spectra are shown in Figure 12c. Similar to L-Phe–$(H_2O)_1$, isomer Aw2-I, in which two waters form cyclic H-bonding with a carboxyl group, is most stable. A good agreement is seen between the calculated and observed IR spectra of Aw2-I. Thus, we conclude that band α′ is due to the cyclic-form L-Phe–$(H_2O)_2$, and the bands in Figure 12c are assigned as follows; the band at 3002 cm^{-1} is the H-bonded carboxyl OH stretch. Those at 3330, and 3474 cm^{-1} are the H-bonded OH stretches of two waters in the H-bond ring, and the bands at 3680 and 3717 cm^{-1} are OH stretches free from the H-bond. The weak and broad bands at ≈3200 cm^{-1} are due to the overlapped transitions of the aromatic CH stretches. One noticeable point in the IR spectrum of L-Phe–$(H_2O)_2$ is that the red-shift of the carboxyl OH stretch with respect to bare L-Phe is as large as 580 cm^{-1}, which is more than twice the red-shift of the OH stretch of phenol–$(H_2O)_2$ and 2-naphthol–$(H_2O)_2$ compared to bare phenol and naphthol,[8,88] indicating that the carboxyl OH is considerably weakened under the hydration of two waters. This can be regarded as favorable for the proton transfer to take place in zwitterion formation.

3.3 Electronic Spectrum and Encapsulation Structure of Calix[4]arene. As was described in the introduction, calixarene (CA) is known as a functional molecule exhibiting encapsulation and self-assembly.[63–65] To date, a variety of substituted calixarenes have been synthesized to improve the ability of encapsulation and recognition of guest molecules. The encapsulation structure and process have been extensively studied in condensed phase, by using NMR and X-ray diffraction methods.[68–70] In the gas phase, mass spectrometry combined with several ion sources, such as electrospray, has been developed for the characterization of encapsulation of charged guests.[76,77] However, most of those experimental studies have been carried out at room temperature and the thermal energy at room temperature is comparable to the non-covalent interaction, so that one generally obtains the averaged information of all possible structures at a given temperature. To understand the intrinsic nature of encapsulation controlled by weak interaction, it is very useful to cool such a host–guest complex in supersonic jet.

3.3.1 Electronic Spectrum of Jet-Cooled Calix[4]arene: The electronic structure of C4A is basically expressed by the linear combination of four phenol and the electronic states of C4A will be ^{1}A, ^{1}E, and ^{1}B under the C_4 point group

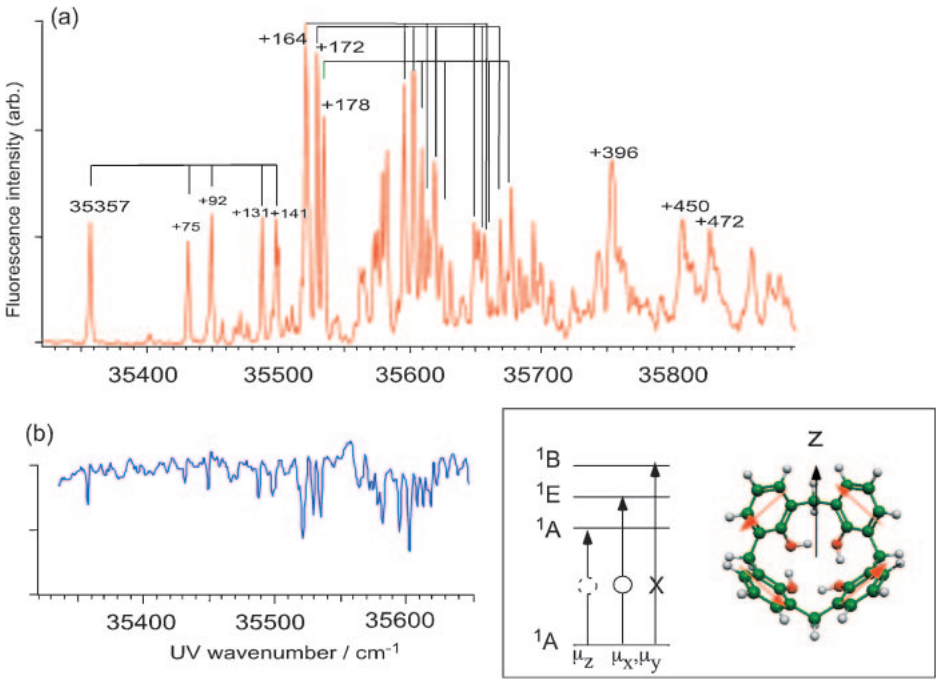

Figure 13. (a) LIF spectrum of C4A in a supersonic jet. (b) UV–UV hole-burning spectrum of C4A obtained by monitoring band origin. Inset: Structure of C4A, electronic states and transition moment of each phenol chromophore building C4A. Figure adapted from Ref. 61.

(Figure 13). Among them, the ^{1}A and ^{1}E states are dipole allowed from the ground state. However, if the transition moment of each phenol is in the x,y-plane (see the inset of Figure 13), the probability of the $^1A \leftarrow S_0(^1A)$ transition becomes zero and only the $^1E \leftarrow S_0(^1A)$ transition has nonzero transition probability. On the other hand, if the transition moment of each phenol moiety is slightly tilted from a perpendicular plane to the C_4 axis, the A ← A transition will have nonzero probability.

Figure 13a shows the LIF spectrum of jet-cooled C4A.[61] In the LIF spectrum, the lowest frequency band at 35357 cm^{-1} is assigned to the band origin, since we do not observe any bands in the lower frequency region under expansion conditions with He carrier gas. In the higher frequency region of the band origin there are four bands up to 35500 cm^{-1}, and three intense bands at 35500–35550 cm^{-1}. For the higher frequency bands, most of the bands appearing in the 35550–35700 cm^{-1} region are assigned to the combination bands, and no prominent progression is seen. The result indicates a large anharmonicity in some of these modes and the existence of intense vibronic coupling in the S_1 state. To examine the possibility of the coexistence of isomers of C4A or other species, we measured UV–UV hole-burning spectrum by fixing the probe laser frequency to the band origin (Figure 13b), and confirmed that only one species is present in the jet.

From the above observation, we discuss the observed electronic state of C4A. In the LIF spectrum of Figure 13a, the intensity of the band origin is weaker than those of the vibronic bands at ≈35530 cm^{-1}. Since we do not see the progression of these vibrations in higher energy regions, those modes are not the totally symmetric mode. Thus, the electronic state can be assigned to the ^{1}A state, and strong bands in the 35530 cm^{-1} region are due to degenerate vibrations with e-symmetry, which appear strongly through a vibronic coupling with the E state which is thought to be located at higher energy.

3.3.2 Encapsulation of Guest Atom by Calix[4]arene: According to DFT calculation at B3LYP/6-31+G* level, the benzene plane of each phenol is tilted by 36 degrees with respect to the $C_4(z)$-axis of C4A, so that a guest molecule or an atom can be captured by four phenols by van der Waals force inside the cavity. We studied an encapsulation of rare gas atoms by C4A. Figure 14a shows the LIF spectra of C4A obtained under expansion with Ar/He mix carrier gas at different mixing ratio. Several new vibronic bands appear by mixing a very small amount of Ar (0.09%) into He carrier gas, and all are red-shifted by 45 cm^{-1} with respect to the monomer bands. The new bands are assigned to those of the C4A–(Ar)$_1$ van der Waals cluster. The magnitude of the red-shift for C4A–Ar$_1$ is larger than that of benzene–(Ar)$_1$ (21 cm^{-1})[94] and phenol–(Ar)$_1$ (34 cm^{-1}).[95]

With an increase of partial pressure of Ar up to 0.75%, the monomer bands become weaker and weaker while additional new bands appear. Typical features are seen in the band origin region and the enlarged portion is shown in Figure 14b. With an increase of Ar partial pressure, the origins of C4A–(Ar)$_{n=2-5}$ appear at lower frequency than C4A–(Ar)$_1$. A notable point is that the magnitudes of the red-shifts for $n \geq 2$ are much smaller than that of $n = 1$; the red-shift $n = 1$ is 45 cm^{-1}, while the additional shifts for $n \geq 2$–5 are 11–4 cm^{-1}. A similar measurement has been carried out for C4A–(Ne)$_n$. Figure 15 shows the plot of the red-shift of the band origins as a function of the number of attached Ar and Ne atoms. The red-shift due to the first atom attachment ($n = 1$) is four times larger than that of the additional shift due to the second atom attachment ($n = 2$), and the shift due to further attachment exhibits a smooth curve with n for $n \geq 2$. The result strongly suggests that the first Ar

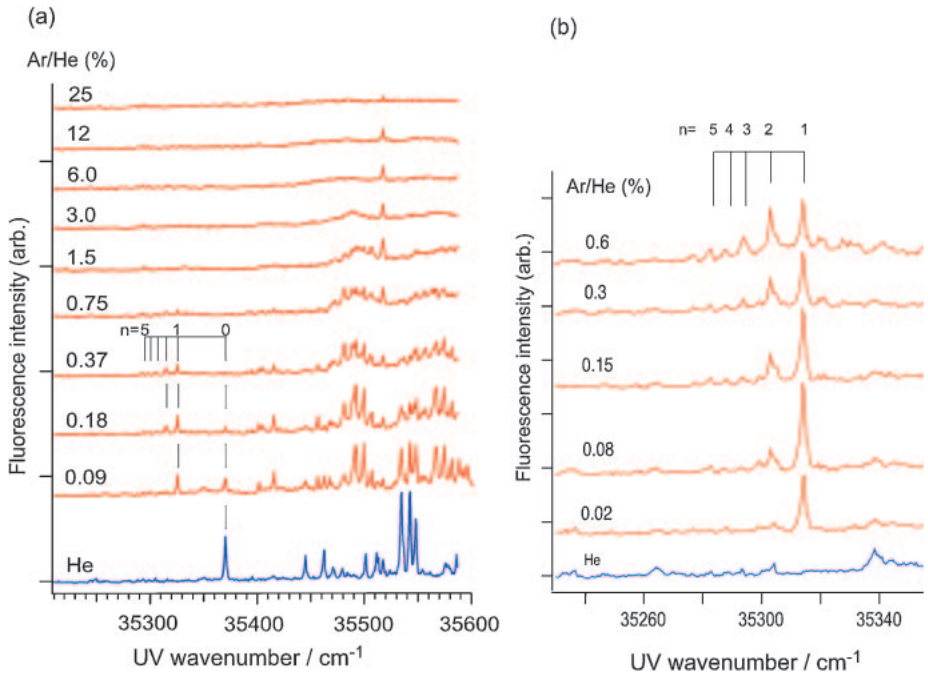

Figure 14. (a) LIF spectrum of C4A–Ar$_n$ clusters at different Ar partial pressures. (b) Expanded view in the band origin region.

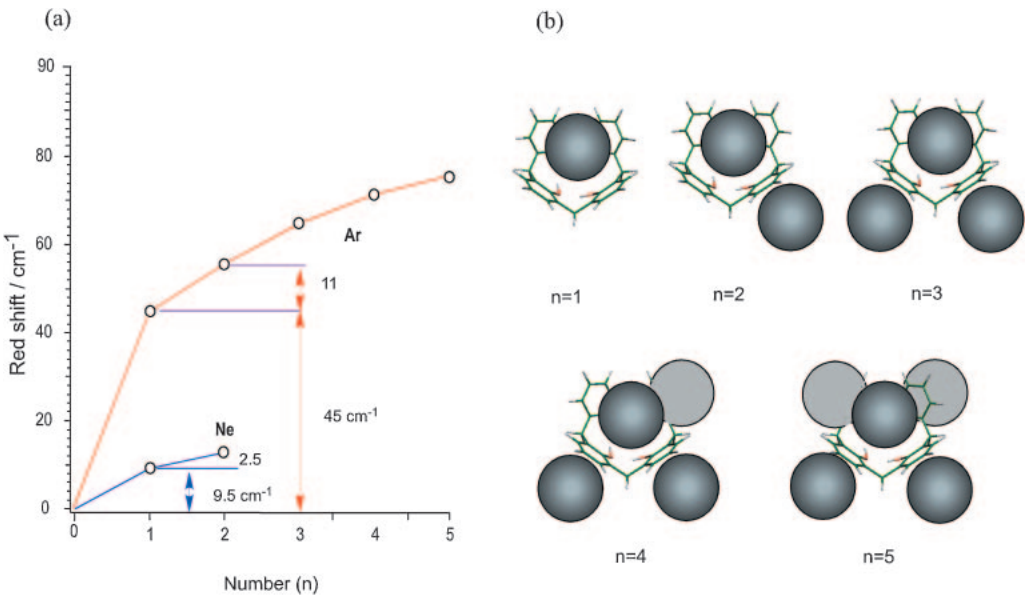

Figure 15. (a) Plot of the red-shift as a function of attached Ar atoms. (b) Proposed structures of C4A–Ar$_n$ clusters.

(Ne) atom is encapsulated inside of the C4A cavity, while additional Ar (Ne) atoms are bound to the outside of the cavity. Our proposed stepwise cluster formation of C4A–(Ar)$_{n=1-5}$ is shown in Figure 15b. For Ne and Ar as a guest, we found that the red-shift is proportional to the polarizability of the guest atom. The observed red-shift of C4A–(Ar)$_1$ and –(Ne)$_1$ is 45 and 9.5 cm^{-1}, respectively, the ratio of which is close to that predicted from the ratio of the polarizabilities of Ne (0.39 Å^3) and Ar (1.62 Å^3).[83] As seen in Figure 15a, the red-shifts for C4A–(Ne)$_n$ show features very similar to those of C4A–(Ar)$_n$, indicating the same structures as C4A–(Ar)$_n$.

3.4 Encapsulation of Water Molecules by Benzo-crown-ethers. Macrocyclic crown ethers are also well-known in host–guest chemistry. The importance of these ethers originates from the remarkable selectivity in encapsulation of guest species. Efficient capture of a guest species can easily be achieved by use of appropriate ethers whose cavity size is similar to that of the guest. Different from calixarene, crown ethers change their conformations due to their flexibility, and adjust the shape of the cavity to accept various kinds of guests. Studies of the conformation and encapsulation of crown ethers have been carried out mostly in liquid phase by various measurements such as elementary analysis, mass spectrometry, optical absorption spectroscopy, and NMR spectroscopy. From a microscopic point of view however, these measurements only show averaged aspects of crown ethers, which are inherent in

condensed phase. For the investigation of the intrinsic nature of the encapsulation, one has to focus attention on the weak intermolecular interaction that strongly controls encapsulation, and jet-cooled spectroscopy is highly suited for the present purpose. We are carrying out laser spectroscopic study on benzo-18-crown-6-ether (B18C6) and dibenzo-18-crown-6-ether (DB18C6) in supersonic jet.[62] In this paper, we describe only DB18C6 (Scheme 1).

3.4.1 Electronic Spectra of DB18C6 and Its Hydrated Clusters: Figure 16a shows the LIF spectrum of jet-cooled DB18C6 in the origin band region.[62] The spectrum is obtained under conditions of high water vapor pressure so that not only bare DB18C6 but also its hydrated clusters coexist. To discriminate different species, UV–UV hole-burning (HB) spectra are measured by monitoring bands **m1**, **m2**, **a**, and **c**–**f** are shown in Figures 16b–16h. From these measurements, bands **m1**, **m2**, **a**, and **c**–**e** in the LIF spectrum are assigned to the origin bands of different species. As to the species belonging to bands **m1** and **m2**, they are due to different conformers of bare DB18C6, because they do not exhibit OH stretching vibration in the IR–UV double resonance spectra, while bands **a**–**f** are identified to originate from hydrated clusters DB18C6–$(H_2O)_n$ because they exhibit OH stretch bands. It should be pointed out that band **m2** is accompanied by a band with an interval of $\approx 5\,cm^{-1}$, while the origin band of **m1** is isolated from other bands. The $5\,cm^{-1}$ doublet structure is also seen in the cluster bands **a** and **c**–**f**.

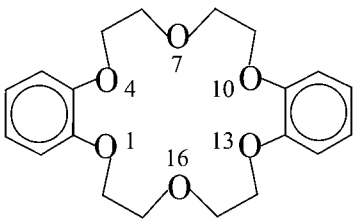

Scheme 1.

3.4.2 Conformation of DB18C6 and Exciton Splitting: We first discuss the conformation of bare DB18C6 corresponding to bands **m1** and **m2**. Three structures are obtained for bare DB18C6 by geometry optimization by DFT calculation at the B3LYP/6-31+G* level (Figure 17). The most stable isomer is a "boat" form belonging to a C_{2v} point group, and the other two conformers are different types of "chair" forms, both of which belong to C_i point groups. We call them "chair I" and "chair II." In Table 1, we list the frequencies of the observed bands **m1** and **m2**, and the $S_1 \leftarrow S_0$ and $S_2 \leftarrow S_0$ transition energies of the three conformers obtained by time-dependent (TD)-DFT calculation at the B3LYP/6-31+G* level. The calculations show that the $S_1 \leftarrow S_0$ transition energy of chair I is the lowest among the three forms, while chair II shows the highest transition energy. The result that the transition energy of chair II is highest in the three conformers can be explained by the difference of the delocalization of the π-orbitals. The electronic transition of DB18C6 is essentially the π–π^* transition of 1,2-dimethoxybenzene (DMB). The π–π^* transition energy decreases when the π-orbitals largely extend to the adjacent O atoms. This delocalization can occur for boat and chair I conformers, because all the atoms of the –C–O–C=C–O–C– frames are in the same planes of the benzene rings. In chair II, on the contrary, the frames are twisted out of the benzene planes, resulting in less delocalization of the π-orbitals and higher $S_1 \leftarrow S_0$ energy than "boat" and "chair I" conformers. Thus, on the basis of the relative energies and transition energies of the three conformers, band **m2** can be assigned to the "boat" conformer and **m1** to the "chair I" conformer.

Here, we discuss the origin of the $5\,cm^{-1}$ doublet for the band **m2**. DB18C6 is constructed by two DMB moieties. The excited states of DB18C6 can be expressed by a linear combination of $\phi_A^* \cdot \phi_B$ and $\phi_A \cdot \phi_B^*$:

$$S_1: \quad \phi_A^* \cdot \phi_B + \phi_A \cdot \phi_B^* \tag{1a}$$

$$S_2: \quad \phi_A^* \cdot \phi_B - \phi_A \cdot \phi_B^* \tag{1b}$$

where ϕ^* and ϕ stand for wave functions of DMB in the S_1 and

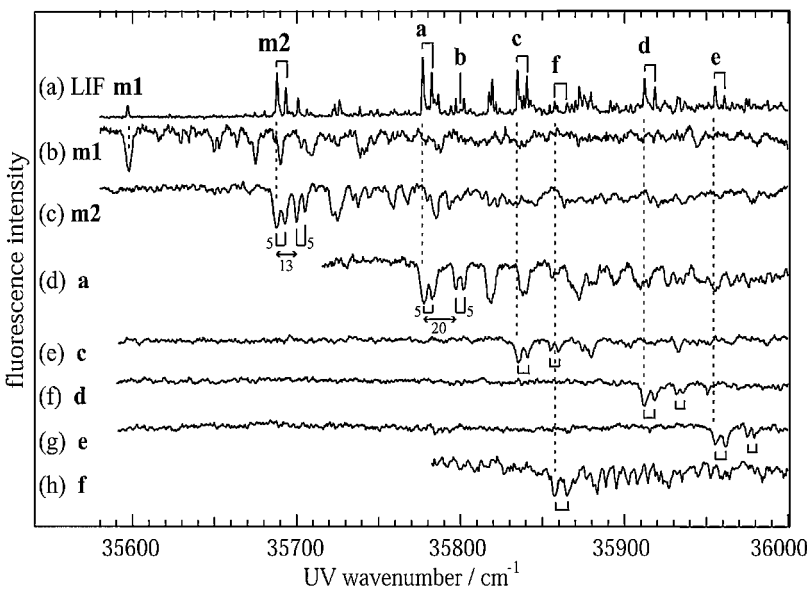

Figure 16. (a) LIF spectrum of DB18C6 and DB18C6–$(H_2O)_n$ in a supersonic jet. (b)–(h) UV–UV hole-burning spectra of DB18C6 and DB18C6–$(H_2O)_n$ obtained by monitoring the bands marked in the LIF spectrum. Figure adapted from Ref. 62b.

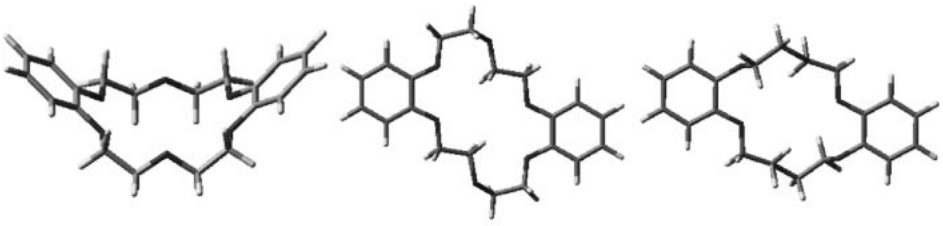

Figure 17. Optimized structures and relative energies of bare DB18C6 obtained by DFT calculation at B3LYP/6-31+G* level. Figure adapted from Ref. 62b.

Table 1. Observed Transition Frequencies (cm^{-1}) of Bands **m1** and **m2** and Calculated Transition Frequencies and Oscillator Strengths of the Corresponding Conformers of DB18C6[a)]

	Transition frequencies (Obsd.)/cm^{-1}		Transition frequencies (Cald.)/cm^{-1}		Oscillator strength (Cald.)	
	S_1-S_0	S_2-S_0	S_1-S_0	S_2-S_0	S_1-S_0	S_2-S_0
m2: boat	35688	35693	39640	39722	0.0928	0.0347
m1: chair I	35597		39608	39688	0.1382	0
Chair II			40133	40145	0.0963	0

a) The calculation is carried out at TD-B3LYP/6-31+G* level.

S_0 states, respectively. For the boat form with C_{2v} symmetry, the transitions from S_0 (A_1) to both the S_1 (B_1) and S_2 (A_1) states are dipole allowed. On the contrary, in the chair form with C_i symmetry, only the transition to the S_1 (A_u) state is dipole allowed. Thus, the 5 cm^{-1} splitting of **m2** can be explained by the S_2–S_1 energy separation of boat-DB18C6, that is the exciton splitting, while the splitting does not appear in **m1** (chair-DB18C6) due to symmetric reasons.

We then estimate the splitting based on the exciton model. In the weak interaction model, the S_2–S_1 splitting energy of a molecule with two equivalent chromophores is given by[96,97]

$$\Delta E = 2FV_{AB} \quad (2)$$

where

$$V_{AB} = \frac{\mu_A \cdot \mu_B}{2\pi\varepsilon_0 {R_{AB}}^3}(2\cos\theta_A\cos\theta_B - \sin\theta_A\sin\theta_B\cos\varphi) \quad (3)$$

R_{AB} is the distance between the two centers of the chromophores, θ_A and θ_B are the angles of the transition dipole moment to the line connecting the two centers, and φ is the dihedral angle between the two transition dipoles. V_{AB} is the electronic part and F is the vibrational part, that is, the Franck–Condon factor. To obtain V_{AB}, we first calculated the oscillator strength for the $S_1 \leftarrow S_0$ transition of DMB at the TD-DFT B3LYP/6-31+G* level. The calculated $S_1 \leftarrow S_0$ oscillator strength of DMB is 0.049, which corresponds to the transition dipole moment of $\mu_{S_1 \leftarrow S_2} = 5.5 \times 10^{-30}$ C m. In boat-DB18C6, the values of θ_A, θ_B, φ, and R_{AB} are 320°, 220°, 0°, and 8.8 Å, respectively. By inserting these values into eqs 2 and 3, we obtain 70 cm^{-1} for $2V_{AB}$. The validity of the estimation of the 70 cm^{-1} S_2–S_1 exciton splitting energy in boat-DB18C6 is supported by the TD-DFT calculation given in Table 1. From the $S_1 \leftarrow S_0$ and $S_2 \leftarrow S_0$ transition energies, we obtain 82 cm^{-1} for the S_2–S_1 energy difference of boat-DB18C6. Estimation of the vibrational part F in eq 2 is difficult, because we do not know the Franck–Condon factor of the $S_1 \leftarrow S_0$ transition. Instead, we estimated F from the relative transition intensity of the origin band in the LIF and UV–UV hole burning spectra of Figures 15a and 15c. The ratio of the origin band LIF intensity to the total LIF intensity is estimated roughly to be ≈10%. This value and $2V_{AB}$ give 7 cm^{-1} for the splitting of band origin (ΔE). Though this estimated value may have a large uncertainty, the value is in reasonable agreement with the experimental observation (5 cm^{-1}). Therefore, the 5 cm^{-1} split of band **m2** can be ascribed to the exciton splitting.

3.4.3 IR Spectra and Structures of DB18C6–$(H_2O)_n$: Since the bands **a**–**f** show a 5 cm^{-1} doublet structure similar to **m2**, the DB18C6 moiety in theses species may have the boat form. The band origins of all the hydrated clusters are blue-shifted and the shift increases with the clusters size. Figures 18a–18f show the IR–UV double resonance spectrum obtained by monitoring bands **a**–**f** in the OH stretching region. Bands **a** and **b** are assigned to different isomers of DB18C6–$(H_2O)_1$. In both spectra, the intensities of the two OH stretch bands are comparable with each other, and their frequencies are lower than the OH vibrations of gas-phase water. Thus, the two OH groups of the water molecule are thought to take the part of double hydrogen donor (bidentate) in the H-bond. In the LIF spectrum, band **a** is located at 89 cm^{-1} higher frequency from band **m2**, which is similar to that of DMB–$(H_2O)_1$ with respect to bare DMB (127 cm^{-1}).[98] In DMB–$(H_2O)_1$, the water molecule is bound to the O atoms of the methoxy groups via two O–H···O hydrogen-bonds. Thus, in the species of band **a** the OH groups of the water molecule are also bonded to the O atoms next to the benzene rings. Band **b** is assigned to another isomer of DB18C6–$(H_2O)_1$ with a bidentate H-bond. The frequencies of the two OH stretching vibrations are slightly higher for **b**, suggesting a weaker bidentate H-bond for band **b** than **a**.

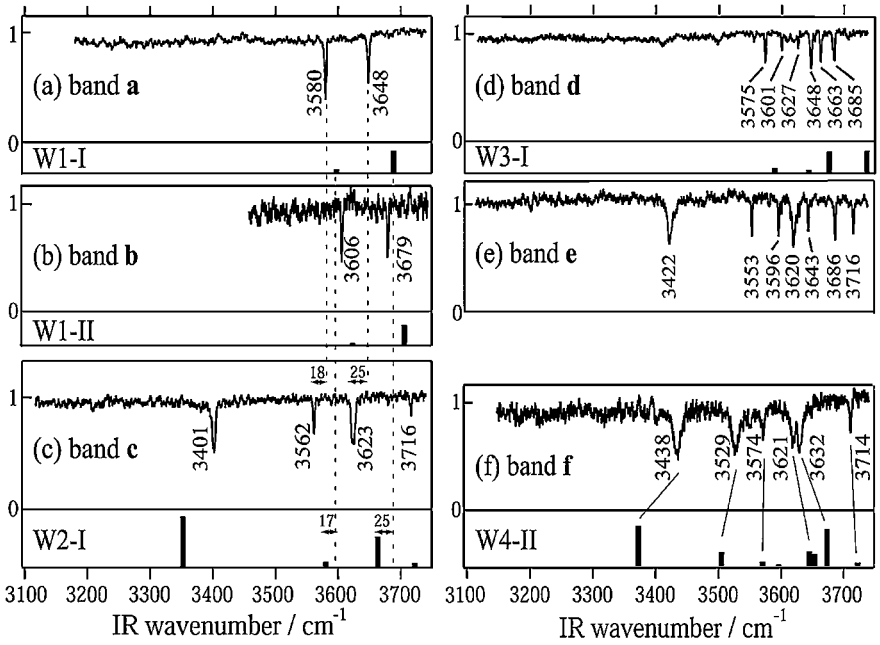

Figure 18. IR–UV double resonance spectra of DB18C6–$(H_2O)_n$ obtained by monitoring the bands (a)–(f) in Figure 17. Stick diagrams are the calculated IR spectrum and the corresponding structures of Figure 19 obtained at B3LYP/6-31+G* level. Figure adapted from Ref. 62b.

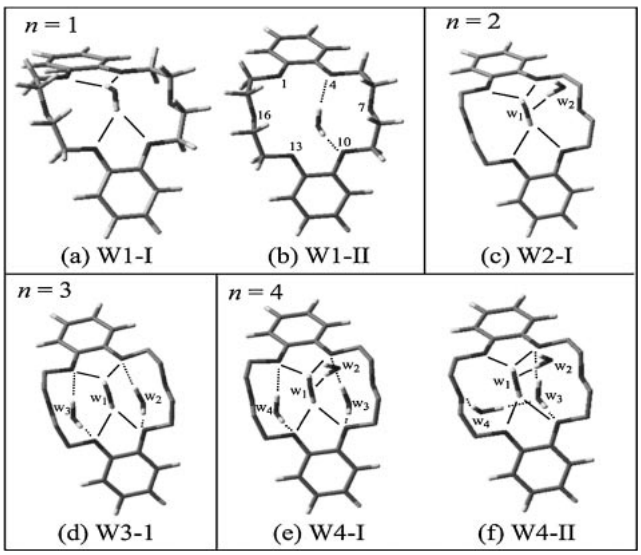

Figure 19. Optimized structures of (a), (b) DB18C6–$(H_2O)_n$, (c) DB18C6–$(H_2O)_2$, (d) DB18C6–$(H_2O)_3$, and (e), (f) DB18C6–$(H_2O)_4$, obtained by DFT calculation at B3LYP/6-31+G* level. Figure adapted from Ref. 62b.

Since it is quite time-consuming to find all the structures by quantum chemical calculations for DB18C6–$(H_2O)_n$, we search particular isomers which are consistent with the observed IR spectra. Figures 19a and 19b shows two optimized structures of DB18C6–$(H_2O)_1$ with boat conformation (W1-I and W1-II). In these structures, a water molecule is H-bonded to the O atoms adjacent to the benzene rings of DB18C6 with the bidentate form. In W1-I, the OH groups of the water molecule point to the middle positions between O_1 and O_4 and between O_{10} and O_{13}, and the cluster has C_{2v} symmetry. In W1-II, the OH groups are pointing directly to O_4 and O_{10}. The IR spectra calculated for W1-I and W1-II are shown in the lower panels of Figures 18a and 18b as a stick diagram. Both W1-I and W1-II display the symmetric and antisymmetric OH stretching vibrations around 3600 and 3700 cm^{-1}, respectively. These IR spectra well coincide with the IR–UV spectra of bands **a** and **b**. We attribute bands **a** and **b** to W1-I and W1-II, respectively, because the OH stretching frequencies of W1-I are slightly lower than those of W1-II.

The IR–UV double-resonance spectrum of band **c** (Figure 18c) shows four OH stretching bands, indicating band **c** to be DB18C6–$(H_2O)_2$. By comparing the IR spectra of band **a** with that of **c**, we assign the IR bands at 3562 and 3623 cm^{-1} in Figure 18c to the symmetric and antisymmetric OH stretching vibrations of a bidentate water, which are red-shifted by 18 and 25 cm^{-1} from those of band **a** (Figure 18a), respectively. The red-shift of the two OH stretching vibrations of the bidentate water implies that the O atom of the bidentate water works as the H-bond acceptor for the next water. The bands at 3401 and 3716 cm^{-1} are assigned to the H-bonded and free OH stretching vibrations of the second water molecule, respectively. The frequency (3401 cm^{-1}) of the H-bonded OH stretch is much lower than that of water dimer H-bond (3530 cm^{-1}).[99] Thus, the H-bond between the two water molecules in band **c** is much stronger than water dimer. Figure 19c shows the most probable structure for the species of band **c** (W2-I). In W2-I, the second water molecule (w_2) is H-bonded to the O atom of the bidentate water molecule (w_1). The IR spectrum calculated for W2-I (stick diagram in Figure 18c) well reproduces the observed spectrum.

Figure 18d shows the IR–UV spectrum of band **d**. The appearance of the six OH stretch bands indicates band **d** to be DB18C6–$(H_2O)_3$. All the bands are located close to each other and no band is observed in the free OH stretch region ($\approx$3715 cm^{-1}). Thus, all the water molecules form a bidentate

H-bond in band **d**. The six bands are classified into three pairs: (1) 3575 and 3648 cm^{-1}, (2) 3601 and 3663 cm^{-1}, and (3) 3627 and 3685 cm^{-1}. The lower and higher frequency bands for each pair are assignable to the symmetric and antisymmetric OH stretching vibrations, respectively. The frequencies of the lowest frequency pair (3575 and 3648 cm^{-1}) are very close to those of band **a** (3580 and 3648 cm^{-1}). Therefore, this pair is assigned to a bidentate water molecule bound to the bottom of the boat-DB18C6. The frequencies of the other two pairs are close to those of band **b** (3606 and 3679 cm^{-1}). Thus, the water molecules for these pairs are thought to form weaker bidentate H-bonds on the top of the boat-form-like W1-II. Figure 19d (W3-I) represents the most probable structure of band **d**. In this structure, one molecule (w_1) is on the bottom side of boat-DB18C6 and forms the bidentate H-bond like W1-I. The other two water molecules (w_2 and w_3) are located on the top and form two bidentate H-bonds to the O atoms near the benzene rings like W1-II. The IR spectrum calculated for W3-I is shown in Figure 18d. Although each of the bands at ≈3650 and ≈3730 cm^{-1} seems to be a single band, there are two close bands assignable to w_2 and w_3 at each position. The positions of the six bands of W3-I agree with those of the IR–UV spectrum of band **d**.

Figure 18e shows the IR–UV spectrum measured by monitoring band **e**. Seven bands are clearly identified and the band at 3620 cm^{-1} has a shoulder. Thus, band **e** is attributed to DB18C6–$(H_2O)_4$. The bands at 3422 and 3716 cm^{-1} are assigned to the H-bonded and free OH stretching vibrations of a single-donor water, respectively. The band positions are similar to the lowest and the highest bands of **c** (Figure 18c, 3401 and 3716 cm^{-1}). Therefore, in the band **e**, there is a single-donor water molecule like w_2 in W2-I. This result also implies that there is a water molecule corresponding to w_1 in W2-I. The bands at 3596, 3643, and 3686 cm^{-1} along with the shoulder of the band at 3620 cm^{-1} suggests that there are two bidentate water molecules in the band **e**. Unfortunately, in our quantum chemical calculations we cannot obtain any optimized isomer of DB18C6–$(H_2O)_4$ whose IR spectrum reproduces the observed IR spectrum. Instead, we present a probable structure (W4-I) of band **e** in Figure 19e.

Figure 18f shows the IR–UV double resonance spectrum of band **f**. The band at 3438 and 3714 cm^{-1} can be assigned to the single-donor OH vibration of a water molecule. The 3529 cm^{-1} band is characteristic in the IR spectrum of band **f**. In Figure 19f (W4-II) is shown a probable structure for band **f**. In W4-II, w_1 and w_2 construct a bidentate and single-donor H-bonded network. The water molecules labeled by w_3 and w_4 are located on the top of boat-DB18C6 and form a new H-bond network. w_3 is bound to the ether O atoms (O_4 and O_{10}) in a bidentate manner, and the other (w_4) forms a bridge between an ether O atom (O_{16}) and the O atom of w_3. This type of H-bond network was also found in the 18-crown-6-ether/water system at liquid nitrogen temperature.[75] The IR spectrum calculated for W4-II displayed in Figure 18f well reproduces the IR–UV spectrum observed for band **f**. In particular, the calculation predicts a band at ≈3500 cm^{-1}, which is the vibration of w_4 H-bonded to the O atom of w_3. This band corresponds to the band at 3529 cm^{-1} in the IR–UV double resonance spectrum of band **f**.

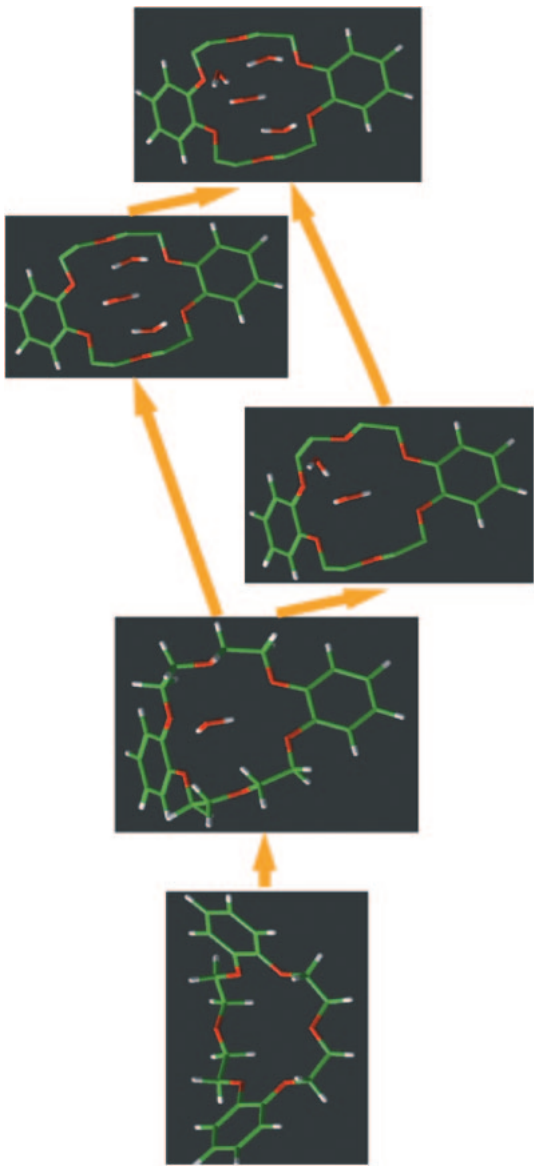

Figure 20. A main route of the growth of H-bonding network of water molecules inside the cavity of DB18C6. Figure adapted from Ref. 62b.

Figure 20 shows a main route of encapsulation of water molecules inside the cavity of DB18C6. First, a water molecule is bound to the oxygen atoms from the bottom of boat-DB18C6 in a bidentate H-bonding form, and the H-bonding network grows on the basis of this structure.

3.5 Picosecond IR–UV Pump–Probe Spectroscopy for Vibrational Energy Relaxation (VE) of the X–H Stretching Vibration. As described above, double resonant vibrational spectroscopy and the combination with quantum chemical calculation enabled us to determine the structure of isolated molecules and size-selected molecular clusters. These studies revealed that the XH stretch vibration exhibits a characteristic feature upon H-bonding, a large red-shift and drastic broadening observed in the condensed phase. A typical example of the effect of the H-bonding on the OH stretching vibration is shown in Figure 21 for H-bonded clusters of *p*-cyanophenol

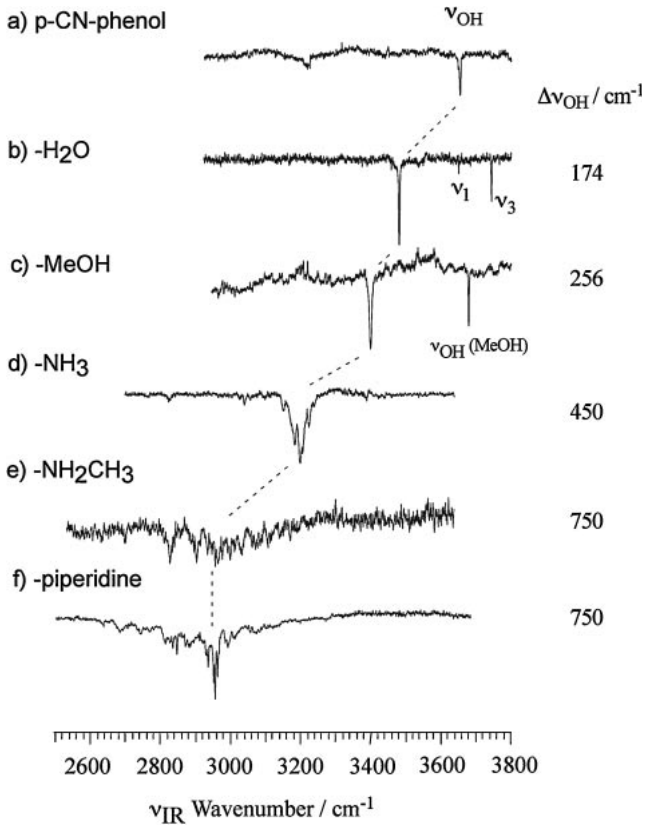

Figure 21. IR–UV double resonance spectra of the H-bonded clusters of *p*-cyanophenol.[100] The red-shift ($\Delta\nu_{OH}$) of the OH stretching vibration in each cluster is shown in units of cm^{-1}.

(*p*-CN–phenol).[100] In these clusters, *p*-CN–phenol acts as the donor and the OH stretching vibration exhibits considerable broadening as well as a large red-shift with an increase in H-bonding. We can perform a molecular level study on the dynamics of the XH stretching vibration of molecules and H-bonded clusters with well characterized structures. We focus our interest on the dynamics of the OH stretching vibration of phenol. We discuss the IVR of the OH stretching vibration of bare phenol and VER of its H-bonded clusters. Here, we employ picosecond IR–UV pump–probe spectroscopy.

Figures 22a and 22b shows the energy levels of bare phenol and its clusters with a picosecond IR–UV pump–probe scheme. The molecules or clusters in the supersonic beam are excited to the OH stretching level by a tunable picosecond IR pulse. The population of the vibrationally excited molecules or clusters is monitored by mass analyzed $1 + 1$ REMPI with a tunable picosecond UV pulse. The $1 + 1$ REMPI spectra from the initial level and doorway states $\{l\}$ show well-resolved sharp bands, while those from dense bath states $\{bath\}$ exhibit broad continuum due to the overlap of many transitions. Therefore, the population of ν_{OH}, $\{l\}$ and $\{bath\}$ can be separately observed by tuning the UV laser to a proper frequency. The time profile of the population is measured by changing the delay time between the IR and the UV pulses. The tunable UV pulse is the second harmonics of an OPG/OPA system (Expra PG401 SH) pumped by a mode-locked picosecond Nd^{3+}:YAG laser (Expra PL2143B). The tunable IR pulse is obtained by a home-made OPG/OPA system. The bandwidth of UV light is 5 cm^{-1} and that of the IR light is 15–20 cm^{-1}. The pulse widths of the pump IR and probe UV lasers were determined to be 12 ps by a cross correlation measurement. The pump–probe signals were convoluted by using the time profiles of the pulses.

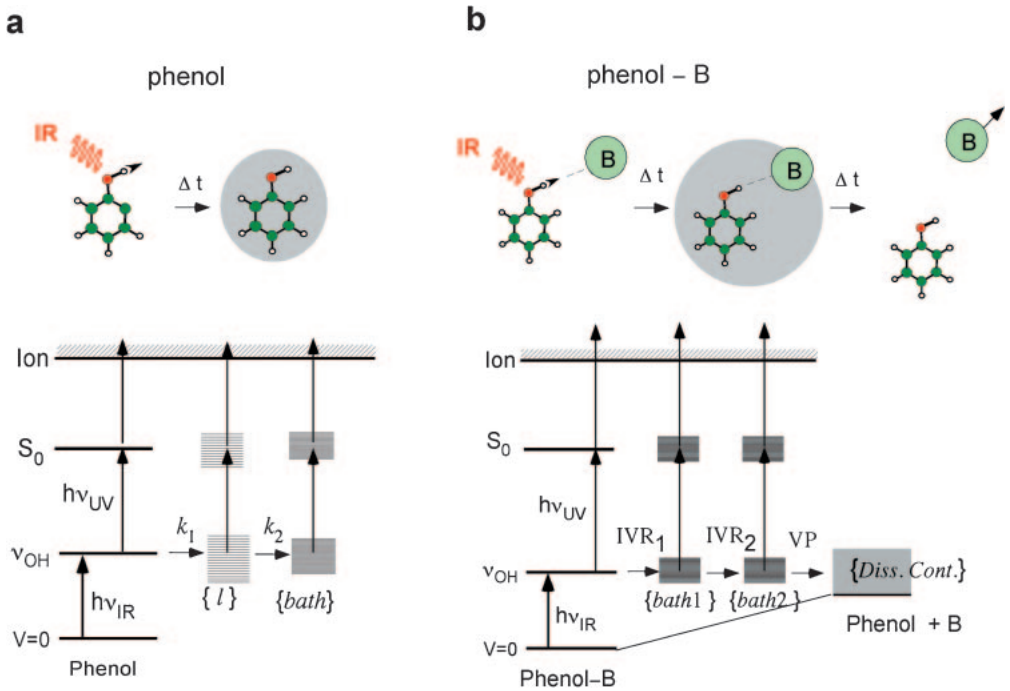

Figure 22. Energy level diagram and vibrational energy flow schemes of (a) bare phenol and (b) H-bonded clusters of phenol in picosecond IR–UV pump–probe spectroscopy.

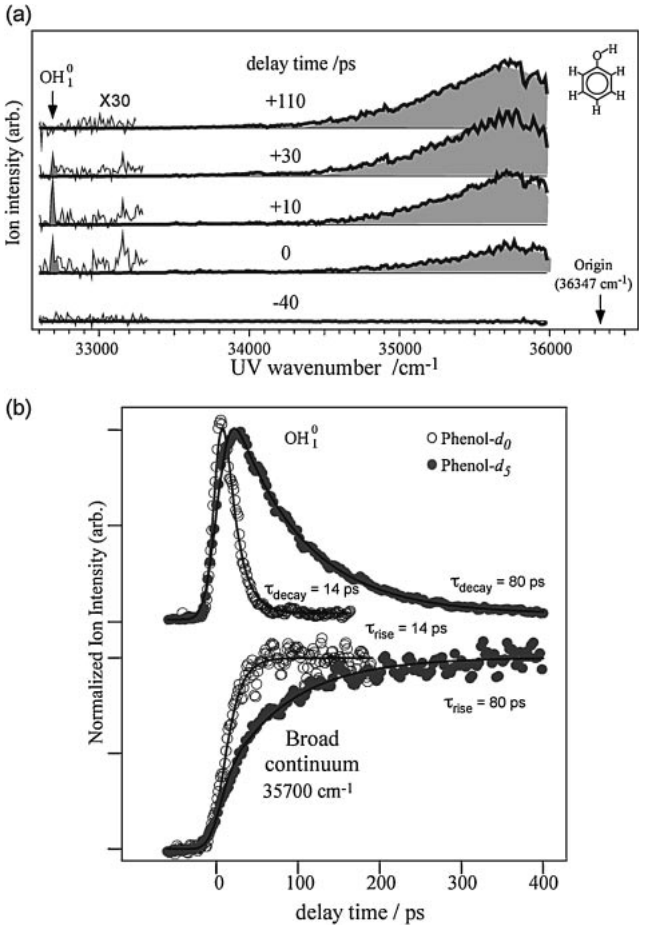

Figure 23. (a) Transient 1 + 1 REMPI spectra of phenol-d_0 after picosecond laser excitation of the OH stretching vibration. (b) Time profiles of the OH_1^0 band and the broad continuum after excitation of the OH stretching vibration of phenol-d_0 (open circle) and phenol-d_5 (solid circle). Solid lines are the convoluted curves by using eqs 4a and 4b. See text.

3.5.1 IVR of the OH(OD) Stretch Vibration of Phenol and Its Isotopomers: 3.5.1.1 OH Stretching Vibration; Figure 23a shows the transient (1 + 1) REMPI spectra of phenol-d_0 (C_6H_5OH) measured at several delay times after exciting the OH stretching vibration at 3657 cm^{-1}.[57] All the UV spectra are shown in the manner that the spectrum observed without the IR laser light is subtracted. At short delay times, several sharp bands, such as the OH_1^0 band (32870 cm^{-1}), are seen in the lower frequency region of the spectra, and they diminish rapidly with the delay time. The broad bands appearing above 34000 cm^{-1} are assigned to the v′–v″ transitions from the dense vibrational levels (v″) generated by IVR from the OH stretch level. Figure 23b shows the time profiles of the OH_1^0 band and broad continuum. A good correlation is seen between the decay of the OH_1^0 band and the rise of the broad continuum. The decay of the OH_1^0 band and the rise of the broad continuum can be fitted by single-exponential decay and rise functions,

$$I_{OH}(t) = I_1 \exp(-t/\tau_{IVR}) \quad (4a)$$

and

$$I_{broad}(t) = I_2\{1 - \exp(-t/\tau_{IVR})\} \quad (4b)$$

by convoluting with the 12 ps width laser pulse shapes. The IVR lifetime is obtained as $\tau_{IVR} = 14$ ps for phenol-d_0. The fact that the decay and the rise can be expressed by an exponential function means that the decay dynamics of the OH stretching vibration of bare phenol belongs to a statistical limit.[101] A similar experiment has been carried out for the OH stretching vibration of phenol-d_5 (C_6D_5OH), which is also shown in Figure 23b. The obtained IVR lifetime is $\tau_{IVR} = 80$ ps for phenol-d_5. Thus, the IVR is drastically reduced by the deuterium substitution of the CH group.

The observed isotope effect suggests the key factors controlling the IVR of the OH stretching vibration in bare phenol. First, the density of states of bath mode is not an important factor to accelerate IVR of the OH stretch, because the vibrational density of states at 3657 cm^{-1} with A′ symmetry is 110/cm^{-1} for phenol-d_0, while it is 350/cm^{-1} for C_6D_5OH (phenol-d_5). The difference predicts much faster IVR for phenol-d_5 than phenol-d_0, which is opposite to the observed IVR lifetimes. This result leads to the conclusion that the OH stretching vibration is not directly coupled with the dense state but is coupled with some special state involving the CH stretch and/or bending vibration. This state can be called "the doorway state."[101–104] The lower panel of Figure 22a shows a model proposed for the IVR process of the OH stretch of bare phenol. The energy flow is described by a two-step tier model,[102–106] that is, "OH stretch level" → "doorway state $\{l\}$" → "dense bath state $\{bath\}$." Here, the decay lifetime of the OH stretch is determined by the "OH stretch ↔ doorway states" coupling, and the present result suggests this coupling strength differs significantly between phenol-d_0 and -d_5. We can further propose that the "doorway state ↔ dense bath states" IVR is much faster than that of "OH stretch ↔ doorway states." In this case, the time constants of the decay of the OH stretch and the rise of the dense state become equal as is observed experimentally. Thus the first IVR step is the rate determining process of the whole IVR process of the OH stretch both in phenol-d_0 and -d_5.

3.5.1.2 OD Stretch Vibration; The OD stretching frequency is 2701 cm^{-1},[107] and density of states at this frequency is reduced to be 15 and 43 states cm for C_6H_5OD (phenol-d_1) and C_6D_5OD (phenol-d_6), respectively. Figure 24a shows the transient UV spectra after exciting the OD stretch vibration of phenol-d_1.[57] The transient spectra exhibit several sharp bands and broad continuum and they show interesting time profiles. Figure 24b shows the time profiles of OD_1^0 band, band A and B. As seen in the figure, the OD_1^0 band and band A(B) show quantum beat with their phase opposite to each other. Bands A and B show the same time profile, indicating they originate from the same level in S_0. Their intensities reach to some constant values at longer delay times.

The time evolutions of bands A and B are really the behavior of the doorway state in the two-step bath mode model. The picosecond IR pulse coherently excites the strongly coupled states in the OD stretch region, producing non-stationary states. The non-stationary states evolve in an oscillatory manner,

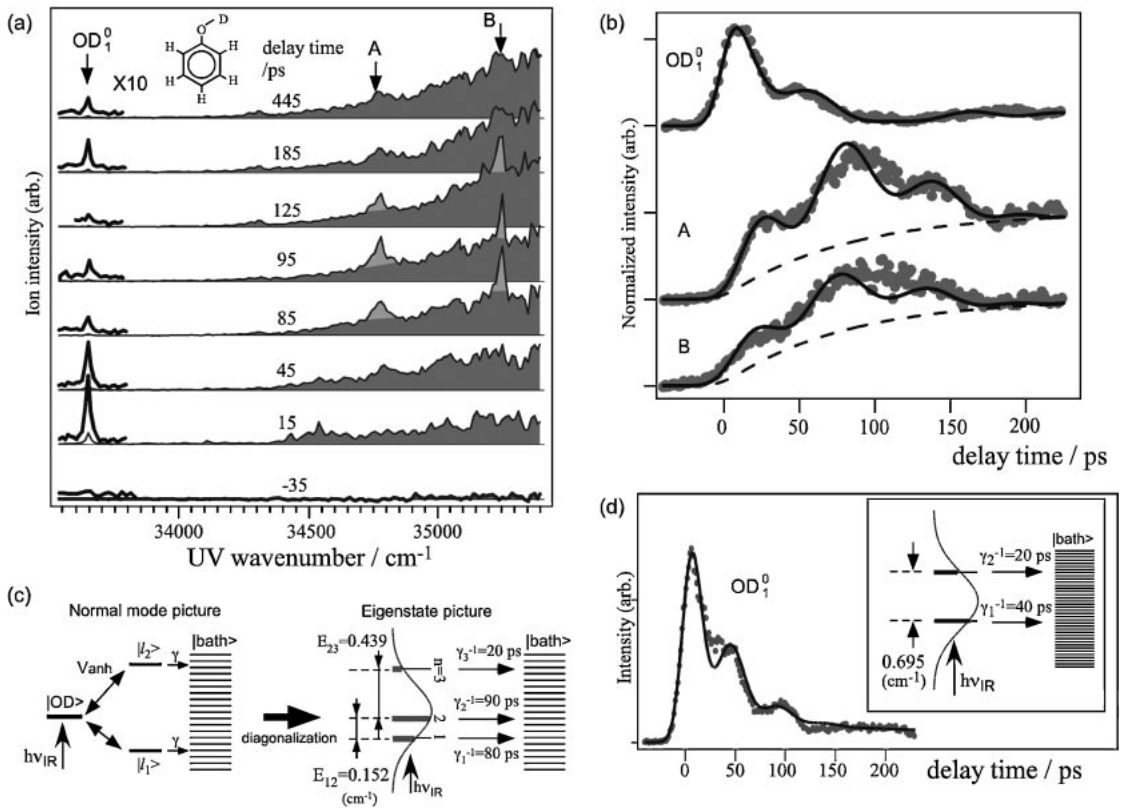

Figure 24. (a) Transient $1+1$ REMPI spectra of phenol-d_1 after picosecond laser excitation of the OD stretching vibration. (b) Time profiles of the OD_1^0 band and bands A and B. Solid curves are the convoluted curves by using eqs 7a and 7b. (c) Coupling scheme of the IVR for the OD stretch of phenol-d_1; (left) Normal mode picture. (right) Eigen state picture. (d) Time profiles of the OD_1^0 band at 33817 cm^{-1} of phenol-d_6. The solid curve is obtained based on the coupling model in the inset. Figure adapted from Ref. 59.

and dissipate into dense bath states,[108–110] as is shown in Figure 24c. In a normal mode picture of this model,[111] the OD stretch level is coupled with the doorway states. The doorway states are coupled further with dense bath states in "pseudo" statistical limit, leading the lifetime of γ^{-1}. The picosecond IR pulse coherently excites the non-stationary states, resulting in a quantum beat with frequencies corresponding to the energy separations. The quantum beat in Figure 24b is composed of oscillations with three different frequencies, which means that the OD stretch vibration is coupled with two doorway states. By using the formulation given in Ref. 108, the quasi-stationary states are expressed as,

$$|n\rangle = \alpha_n|\mathrm{OD}\rangle + \sum_{m=1}^{2}\beta_n^{l_m}|l_m\rangle \tag{5}$$

Here, $|\mathrm{OD}\rangle$ and $|l_m\rangle$ denote the OH stretch and the doorway states in the zero-th order, respectively, and α_n and $\beta_n^{l_m}$ are the coefficients. The time evolution of the coherently excited quasi-stationary states is expressed as

$$|\varphi(t)\rangle = \sum_{n=1}^{3}\alpha_n|n\rangle \mathrm{e}^{-i\frac{\varepsilon_n}{\hbar}t} \tag{6}$$

In eq 6, $\varepsilon_n = E_n - \frac{i}{2}\gamma_n$, where E_n is the energy of the stationary state and γ_n is its width. The time profiles of the OD stretch, one of the doorway states, and the dense bath states are given by

$$|\langle \mathrm{OD}|\varphi(t)\rangle|^2 = \sum_{n=1}^{3}|\alpha_n|^4\mathrm{e}^{-\frac{\gamma_n}{\hbar}t} + 2\sum_{n\neq m}|\alpha_n|^2|\alpha_m|^2\cos\left(\frac{E_{nm}}{\hbar}t\right)\mathrm{e}^{-\frac{\gamma_n+\gamma_m}{2\hbar}t} \tag{7a}$$

$$|\langle l_1|\varphi(t)\rangle|^2 = \sum_{n=1}^{3}|\alpha_n|^2|\beta_n^{l_1}|^2\mathrm{e}^{-\frac{\gamma_n}{\hbar}t} + 2\sum_{n\neq m}\alpha_n\alpha_m\beta_n^{l_1}\beta_m^{l_1}\cos\left(\frac{E_{nm}}{\hbar}t\right)\mathrm{e}^{-\frac{\gamma_n+\gamma_m}{2\hbar}t} \tag{7b}$$

and

$$\mathrm{Bath}(t) = 1 - \sum_{n=1}^{3}|\alpha_n|^2\mathrm{e}^{-\frac{\gamma_n}{\hbar}t} \tag{7c}$$

respectively, with $\gamma_n = (1-|\alpha_n|^2)\gamma$. Here Bath($t$) is the population of the dense bath states. The coefficients (α_n), energy separations (E_{nm}), and widths (γ) are determined by fitting the time profile of eq 7a to the observed profile of the OD_1^0 band. We assumed that γ's are equal for the two doorway states and that of OD stretch is negligibly small. The obtained coefficients and width are $\alpha_1 = 0.152$, $\alpha_2 = 0.663$, $\alpha_3 = 0.424$, and $\gamma = (50\,\mathrm{ps})^{-1}$. The energy spacing and γ_n are shown in Figure 24c. The coefficients ($\beta_n{}^{l1}$) are obtained by fitting the time profile of eq 7b to the observed profile of band A, and they are $\beta_1{}^{l1} = 0.784$, $\beta_2{}^{l1} = -0.465$, and $\beta_3{}^{l1} = -0.411$. The

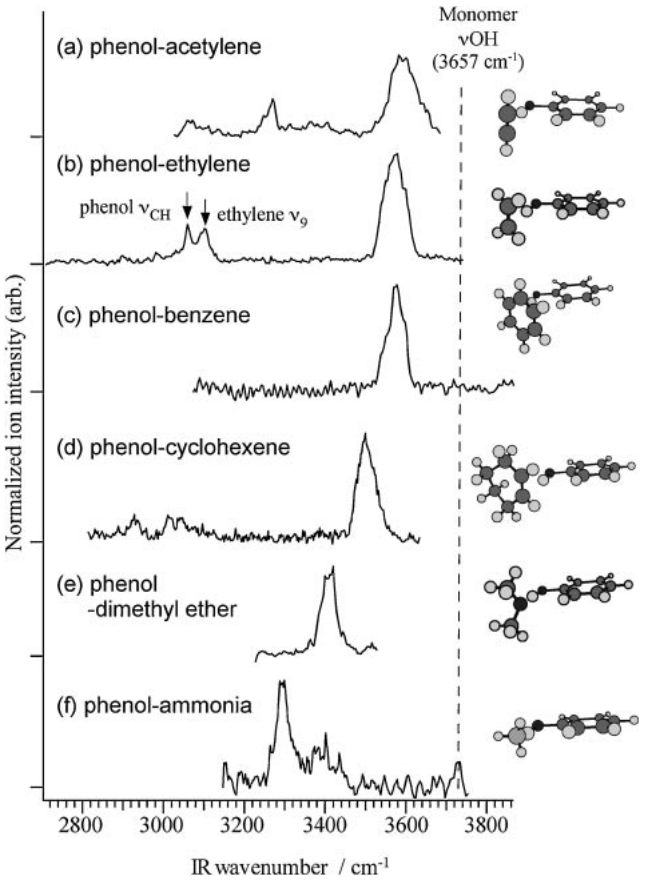

Figure 25. (Left) Ion gain IR spectra of H-bonded clusters of phenol observed by picosecond IR–UV pump–probe spectroscopy. (Right) Optimized structures of the corresponding clusters. Figure adapted from Ref. 38c.

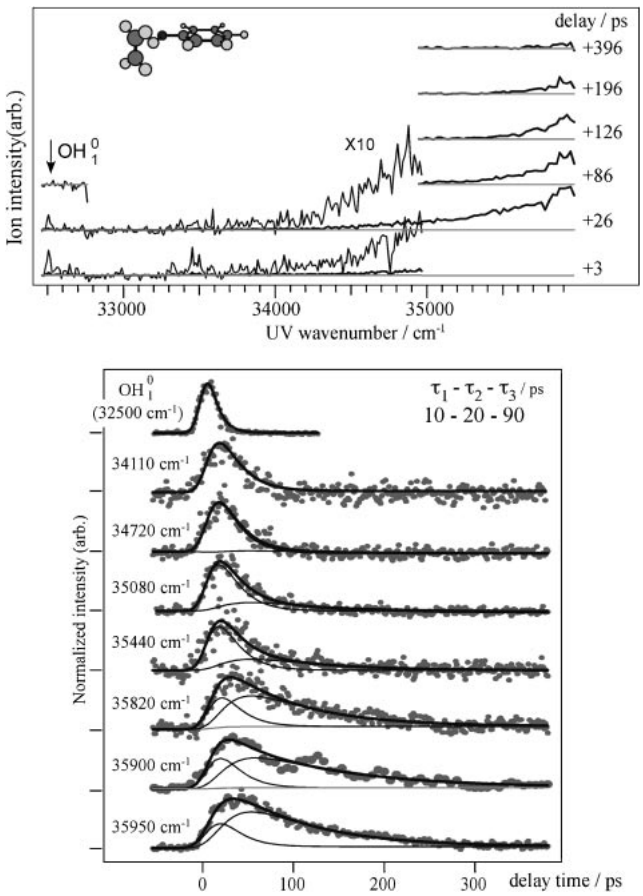

Figure 26. (Upper) Transient $1+1$ REMPI spectra of phenol–ethylene H-bonded cluster after the picosecond laser excitation of the OH stretching vibration. (Lower) Time profiles of the OH_1^0 band and broad continuum. Solid lines are the convoluted curves by suing eqs 9a, 9b, and 9c. See text. Figure adapted from Ref. 58.

good agreement between the observed and the calculated time profiles (solid curves) for the OD_1^0 and band A shows the validity of the model.

The quantum beat is also observed in the IVR of the OD stretch of phenol-d_6 (Figure 24d). The $OD^0{}_1$ band exhibits a single frequency beat, so only one state is coupled with the OD stretch. The convoluted curve is also shown as the solid curve in Figure 24d, and the energy levels are shown in the inset. For phenol-d_6, the obtained values are $\alpha_1 = 0.806$, $\alpha_2 = 0.592$, and $\gamma = (15\,\mathrm{ps})^{-1}$. In the case of phenol-$d_6$, we could not observe any sharp transitions from the doorway state.

3.5.2 IVR and VP of Phenol Clusters: The lower panel of Figure 22b shows the energy level diagram of a phenol cluster and our proposed relaxation scheme, which will be discussed later. Essentially, the OH stretching vibration of the clusters is excited by the picosecond IR pulse. After certain delay times, the transient $1+1$ REMPI spectrum is observed. The time evolution of the pumped OH level is observed as the OH_1^0 band, and those of the levels (v'') generated by IVR are observed as the $v' \leftarrow v''$ transitions. The latter transitions exhibit broad continuum similar to the case of bare phenol. In the cluster, the input IR energy (3000–3600 cm^{-1}) is large enough to dissociate the H-bonding. Thus the cluster disappears due to the vibrational predissociation (VP), which reflects in the decay of the broad continuum. Figure 25 shows the IR spectra of various 1:1 H-bonded clusters of phenol in the OH stretching region and the optimized structures. All the IR spectra are obtained as ion-gain spectra, in which the UV frequency is fixed to the transition from the IVR redistributed levels and the IR frequency is scanned. Phenol forms a π-type H-bond with acetylene (Ac), ethylene (Et), benzene (Bz), and cyclohexene (cHe), while it forms a σ-type H-bond with dimethyl ether (DME) and ammonia (Am). In the following, we examine the effects of the H-bonding strength as well as the mass of the acceptor molecule on the dynamics of the OH stretching vibration by measuring the transient UV spectra.

Upper traces of Figure 26 show the transient UV ($1+1$ REMPI) spectra of phenol–Et clusters measured at several delay times after IR excitation of the H-bonded OH stretch vibration.[59] Each spectrum is shown in the manner that the $1+1$ REMPI spectrum without the IR laser irradiation is subtracted. In all the spectra, sharp vibronic bands originating from $v_{OH} = 1$, such as OH_1^0 at 32500 cm^{-1}, rapidly disappear. A broad continuum appearing in the region higher than 34000 cm^{-1} is assigned to the transitions from the dense levels generated by IVR of the OH stretch vibration. The continuum shows rapid rise coincident with the decay of OH_1^0, and diminishes in a few hundreds picoseconds, which is due to the

dissociation of the H-bond. Lower traces of Figure 26 show the time profiles of the OH_1^0 band and the broad continuum. The OH_1^0 band disappears within 30 ps. The broad transitions, on the other hands, reach to the maxima at 30–50 picoseconds and disappear at ≈300 picoseconds. An important point is that the decay time profile of the broad continuum shows UV frequency dependence. For example, the signal observed at $\nu_{UV} = 34110\,cm^{-1}$ reaches the maximum at 17 ps and disappears at 100 ps, while the signal at $\nu_{UV} = 35950\,cm^{-1}$ reaches to the maximum at 30 ps and disappears at 300 ps. This tendency is seen in all the clusters investigated, and is in accordance with the behavior of the transient UV spectra described above.

The UV frequency dependence of the time profile of the broad continuum, that is the transitions from the redistributed levels, indicates that the mechanism of energy flow from the OH stretch level is not a simple two-step model assuming VP via one bath mode, which gives the following time behavior for the OH stretch and the bath mode.

$$I_{OH}(t) = C_p e^{-k_1 t} \tag{8a}$$

and

$$I_{bath}(t) = C_b(-e^{-k_1 t} + e^{-k_2 t}) \tag{8b}$$

where k_1 $(=1/\tau_{IVR})$ is the IVR rate constant of the OH stretching level and k_2 $(=1/\tau_{diss})$ is the H-bond dissociation rate constant from the bath mode. C_p and C_b are the constants including the laser intensity, the S_1–S_0 absorption cross-section, and the ionization efficiency. In this scheme the time profile of the bath mode, $I_{bath}(t)$, is independent of the monitoring UV frequency, which does not agree with the observed results.

The observed time profile of the broad continuum can be described by a "two bath modes model" (lower pannel of Figure 22b). In this model, the OH stretching level first relaxes to "bath (1)" with the rate constant k_1 $(=1/\tau_{IVR1})$, and "bath (1)" further relaxes to "bath (2)" with the rate constant k_2 $(=1/\tau_{IVR2})$. The cluster in "bath (2)" dissociates with the rate constant k_3 $(=1/\tau_{VP})$. The time profiles of the OH level, the bath (1) and the bath (2) are expressed as follows,

$$I_{OH}(t) = C_p e^{-k_1 t} \tag{9a}$$

$$I_{bath(1)}(t) = C_{b1}(-e^{-k_1 t} + e^{-k_2 t}) \tag{9b}$$

$$I_{bath(2)}(t) = C_{b2}\{(k_1 - k_2)e^{-k_3 t} - (k_1 - k_3)e^{-k_2 t} + (k_2 - k_3)e^{-k_1 t}\} \tag{9c}$$

The transient UV spectrum involves both the transitions of bath (1) and (2), and their relative intensity is different at the different frequency so that the profile of the transient UV spectrum should be frequency dependent. The pump–probe signals observed in the lower frequency region showed faster decay than that observed at higher frequency. This means that at lower UV frequency "bath (1)" has greater intensity than that of bath (2), that is $C_{b1}/C_{b2} > 1$. On the other hand, the ratio is reversed at high UV frequency, that is $C_{b1}/C_{b2} < 1$. So we fitted the curve by combining the two components, $I_{bath(1)}$ and $I_{bath(2)}$, with changing parameters, k_2, k_3, and C_{b1}/C_{b2}, as shown in Figure 26. Here, time profiles of each component are shown as thin curves and the total time profile is shown as a thick curve.

Here, we comment on the meaning of "baths (1) and (2)" in the proposed model, and discuss the energy flow mechanism in the H-bonded clusters. As seen in Figure 26, the broad continuum observed at short delay times is widely extended more than $2000\,cm^{-1}$ below the band origins of the clusters. Such a large red-shift can only be explained by that the transition mainly involves $\Delta v = -1$, -2, and -3 transitions of Franck–Condon active modes of phenolic moiety. On the other hand, the electronic transitions of the intermolecular mode should appear close to the 0,0 band. This is because the frequencies of intermolecular modes are less than $200\,cm^{-1}$ and the largely red-shifted electronic transition, corresponding to the large change of Δv, should have very small Franck–Condon factors. This result strongly indicates that the OH stretching vibrational energy is initially redistributed within the phenolic site of the cluster, which corresponds to bath (1). Then the energy in bath (1) is further relaxed to bath (2) which mainly consists of low-frequency intermolecular vibrational mode. This is the reason why the higher frequency part of the broad electronic transition remained even at longer delay time. Thus, the energy flow scheme from the phenolic OH stretching vibration can be given by the following scheme,

$$\begin{aligned}\text{Ph(OH)}^*\text{–acceptor} &\rightarrow \text{(PhOH)}^*\text{–acceptor} \\ &\rightarrow \text{(PhOH–acceptor)}^* \rightarrow \text{PhOH} + \text{acceptor}\end{aligned} \tag{10}$$

Here Ph(OH)*, (PhOH)*, and (PhOH–acceptor)* are the phenol with the OH stretch excited, the internally excited phenol, and the internally excited cluster, respectively.

Figure 27 shows the plot of the rate constant of each step against the red-shift of OH stretch.[112] The red-shifts of the π-type H-bonding are 50–120 cm^{-1}, while those of σ-type H-bonding are estimated to be 180–300 cm^{-1}, depending on the basicity (or proton affinity) of the acceptor. Thus, the red-shift of the OH stretch is a good measure of the H-bonding strength. The rate constant of the initial-step, k_1, shows a clear H-bonding strength dependence, indicating that the H-bonding accelerates the "IVR within the phenolic site (IVR1)." On the other hand, the rate constants of the other two processes do not show a clear correlation with the H-bond strength. Thus, the "OH stretch ↔ intramolecular vibrational mode" coupling is strongly enhanced by the increase of the H-bond strength, while the effect of the H-bonding strength on the "intramolecular ↔ intermolecular" mode coupling and the "intermolecular mode ↔ dissociation continuum" coupling is small. The reason why IVR1 depends on the H-bonding strength can be explained by that the large reduction of the OH stretching frequency drastically changes the anharmonic coupling strength between the OH stretch and the bath (1) composed of the vibrations of the CH group, such as the CH stretch. With the decrease of the OH stretch, the energy gap between the OH stretch and the CH stretch becomes smaller, leading to the increase of the "OH stretch ↔ bath (1)" anharmonic coupling expected by the energy gap law.[30,113] On the other hand, the change of the CH stretch frequency upon the H-bonding is very small so that the effect of the H-bond on the "bath (1) ↔ bath (2)" coupling is also vey small. In addition, IVR2 and VP processes consist of multiple orders of the couplings involving many vibrational levels, and they are not so different for different H-bonding clusters. Those reasons may explain why

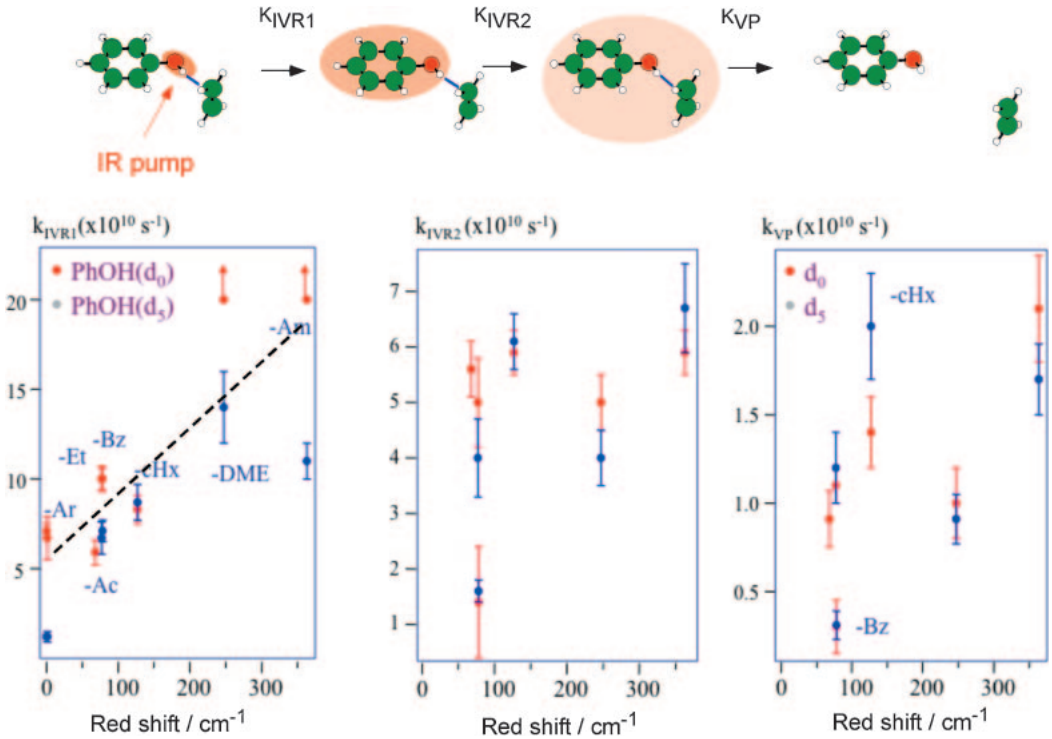

Figure 27. (upper) VER scheme of the H-bonded cluster of phenol. (lower) Plot of the rate constant of each IVR step of the H-bonded clusters of phenol vs. the red-shift of the OH stretching vibration.[112]

IVR2 and VP do not sensitively depend on the H-boding strength.

Conclusion

The structure and dynamics of gas-phase aromatic molecules and their clusters has been studied by size- and conformer-selective double resonance vibrational spectroscopy. IR–UV and stimulated Raman–UV double resonance spectroscopy have been applied. In these methods, the depletion of the ground state population induced by intense tunable IR laser light or stimulated Raman pumping is monitored by laser-induced fluorescence and resonance-enhanced multiphoton ionization spectroscopy having a high selectivity of the conformer and size as well as a high sensitivity. An application of these spectroscopies to several vibrations ranging from 0 to 3700 cm^{-1} has been demonstrated for the H-bonded clusters of benzonitrile. A conformer selective vibrational spectroscopy was demonstrated for L-phenylalanine and its hydrated cluster. We also showed our recent study on the encapsulation structure of guest atom and molecules by functional molecules, calixarene and crown ether. In the time domain study, pico-second IR–UV pump–probe spectroscopy was applied to study the vibrational energy relaxation (VER) of isolated aromatic molecules and the H-bonded clusters. We showed clear evidence that IVR of the OH stretch proceeds via the doorway state in the bare molecule. This intramolecular process is also a very important step in the whole VER process of the H-bonded clusters, that is VER occurs with the following steps, "OH stretch" → "intramolecular vibrational energy redistribution" → "intracluster vibrational energy redistribution" → "H-bond dissociation."

The author express special thank to Profs. N. Mikami, A. Fujii, Y. Inokuchi, and Dr. Y. Yamada as collaborators through these works. This work is supported by JSPS through a Grant-in-Aid project (Nos. 18205003 and 19655004) and by the MEXT, Japan through the Grant-in-Aid for the Scientific Research on Priority Area "Molecular Science for Supra Functional Systems" (No. 477).

References

1 a) F. Huisken, A. Kulcke, C. Laush, J. M. Lisy, *J. Chem. Phys.* **1991**, *95*, 3924. b) F. Huisken, M. Stemmler, *J. Chem. Phys.* **1993**, *98*, 7680. c) F. Huisken, M. Kaloudis, A. Kulcke, *J. Chem. Phys.* **1996**, *104*, 17.

2 U. Buck, H. Meyer, *Phys. Rev. Lett.* **1984**, *52*, 109.

3 a) N. Pugliano, J. D. Cruzan, J. G. Loeser, R. J. Saykally, *J. Chem. Phys.* **1992**, *98*, 6600. b) J. B. Paul, C. P. Collier, J. J. Saykally, J. J. Scherer, A. O'Keefe, *J. Phys. Chem. A* **1997**, *101*, 5211. c) K. Liu, M. G. Brown, R. J. Saykally, D. Clary, *Nature* **1996**, *391*, 591.

4 a) C. Riehn, C. Lahmann, B. Wessermann, B. Brutschy, *Chem. Phys. Lett.* **1992**, *197*, 443. b) C. Riehn, C. Lahmann, B. Wessermann, B. Brutschy, *Ber. Bunsenges. Phys. Chem.* **1992**, *96*, 1161.

5 a) R. H. Page, Y. R. Shen, Y. T. Lee, *J. Chem. Phys.* **1988**, *88*, 4621. b) R. H. Page, Y. R. Shen, Y. T. Lee, *J. Chem. Phys.* **1988**, *88*, 5362.

6 a) P. Esherick, A. Owyoung, *Chem. Phys. Lett.* **1983**, *103*, 235. b) P. Esherick, A. Owyoung, J. Plíva, *J. Chem. Phys.* **1985**, *83*, 3311. c) J. Plíva, P. Esherick, J. Owyoung, *J. Mol. Spectrosc.* **1987**, *125*, 393.

7 a) V. A. Venturo, P. M. Felker, *J. Chem. Phys.* **1993**, *99*, 748. b) M. W. Schaeffer, P. M. Maxton, P. M. Felker, *Chem. Phys.*

Lett. **1994**, *224*, 544. c) M. W. Schaeffer, W. Kim, P. M. Maxton, J. Romascan, P. M. Felker, *Chem. Phys. Lett.* **1995**, *242*, 632. d) G. V. Hartland, B. F. Henson, V. A. Venturo, P. M. Felker, *J. Phys. Chem.* **1992**, *96*, 1164.

8 a) S. Tanabe, T. Ebata, M. Fujii, N. Mikami, *Chem. Phys. Lett.* **1993**, *215*, 347. b) N. Mikami, *Bull. Chem. Soc. Jpn.* **1995**, *68*, 683. c) T. Watanabe, T. Ebata, S. Tanabe, N. Mikami, *J. Chem. Phys.* **1996**, *105*, 408. d) T. Ebata, A. Fujii, N. Mikami, *Int. J. Mass Spectrom. Ion Processes* **1996**, *159*, 111.

9 a) R. N. Pribble, T. S. Zwier, *Science* **1994**, *265*, 75. b) R. N. Pribble, T. S. Zwier, *Faraday Discuss.* **1994**, *97*, 229. c) C. J. Gruenloh, J. R. Carney, C. A. Arrington, T. S. Zwier, S. Y. Fredericks, K. D. Jordan, *Science* **1997**, *276*, 1678.

10 For example, see: H. Watanabe, S. Iwata, *J. Chem. Phys.* **1996**, *105*, 420.

11 Since there have been so many papers on double resonance vibrational spectroscopy of molecular clusters, only review papers are cited here: a) T. Ebata, A. Fujii, N. Mikami, *Int. Rev. Phys. Chem.* **1998**, *17*, 331. b) T. S. Zwier, *Annu. Rev. Phys. Chem.* **1996**, *47*, 205. c) B. Brutschy, *Chem. Rev.* **2000**, *100*, 3891.

12 L. C. Snoek, R. T. Kroemer, M. R. Hockridge, J. P. Simons, *Phys. Chem. Chem. Phys.* **2001**, *3*, 1819.

13 L. C. Snoek, R. T. Kroemer, J. P. Simons, *Phys. Chem. Chem. Phys.* **2002**, *4*, 2130.

14 L. I. Grace, R. Cohen, T. M. Dunn, D. M. Lubman, M. S. de Vries, *J. Mol. Spectrosc.* **2002**, *215*, 204.

15 I. Hünig, A. J. Painter, R. A. Jockusch, P. Çarçabal, E. M. Marzluff, L. C. Snoek, D. P. Gamblin, B. G. Davis, J. P. Simons, *Phys. Chem. Chem. Phys.* **2005**, *7*, 2474.

16 P. Çarçabal, T. Patsias, I. Hünig, B. Liu, C. Kaposta, L. C. Snoek, D. P. Gamblin, B. G. Davis, J. P. Simons, *Phys. Chem. Chem. Phys.* **2006**, *8*, 129.

17 J. Oomens, N. Polfer, D. T. Moore, L. van der Meer, A. G. Marshall, J. R. Eyler, G. Meijer, G. von Helden, *Phys. Chem. Chem. Phys.* **2005**, *7*, 1345.

18 N. A. Macleod, P. Butz, J. P. Simons, G. H. Grant, C. M. Baker, G. E. Tranter, *Phys. Chem. Chem. Phys.* **2005**, *7*, 1432.

19 T. Hashimoto, Y. Takasu, Y. Yamada, T. Ebata, *Chem. Phys. Lett.* **2006**, *421*, 227.

20 T. Ebata, T. Hashimoto, T. Ito, Y. Inokuchi, F. Altunsu, B. Brutschy, P. Tarakeshwar, *Phys. Chem. Chem. Phys.* **2006**, *8*, 4783.

21 Y. Inokuchi, Y. Kobayashi, T. Ito, T. Ebata, *J. Phys. Chem. A* **2007**, *111*, 3209.

22 A. Laubereau, W. Kaiser, *Rev. Mod. Phys.* **1978**, *50*, 607.

23 D. J. Nesbitt, R. W. Field, *J. Phys. Chem.* **1996**, *100*, 12735.

24 T. Elsaesser, W. Kaiser, *Annu. Rev. Phys. Chem.* **1991**, *42*, 83.

25 R. M. Stratt, M. Maroncelli, *J. Phys. Chem.* **1996**, *100*, 12981.

26 E. J. Heilweil, M. P. Casassa, R. R. Cavanagh, J. C. Stephenson, *J. Chem. Phys.* **1986**, *85*, 5004.

27 J. R. Ambroseo, R. M. Hochstrasser, *J. Chem. Phys.* **1988**, *89*, 5956.

28 M. M. Heckscher, L. Sheps, D. Bingemann, F. F. Crim, *J. Chem. Phys.* **2002**, *117*, 8917.

29 C. G. Elles, M. J. Cox, F. F. Crim, *J. Chem. Phys.* **2004**, *120*, 6973.

30 A. Nitzan, S. Mukamel, J. Jortner, *J. Chem. Phys.* **1975**, *63*, 200.

31 D. J. Myers, M. Shigeiwa, M. D. Fayer, B. J. Cherayil, *J. Phys. Chem. B* **2000**, *104*, 2402.

32 a) V. M. Kenkre, A. Tokmakoff, M. D. Fayer, *J. Chem. Phys.* **1994**, *101*, 10618. b) I. J. Finkelstein, J. Zheng, H. Ishikawa, S. Kim, K. Kwak, M. D. Fayer, *Phys. Chem. Chem. Phys.* **2007**, *9*, 1533.

33 a) H. J. Bakker, *J. Chem. Phys.* **1993**, *98*, 8496. b) S. Woutersen, U. Emmerichs, H.-K. Nienhuys, H. J. Bakker, *Phys. Rev. Lett.* **1998**, *81*, 1106. c) H. J. Bakker, *J. Chem. Phys.* **2004**, *121*, 10088.

34 a) H. S. Yoo, M. J. DeWitt, B. H. Pate, *J. Phys. Chem. A* **2004**, *108*, 1348. b) H. S. Yoo, M. J. DeWitt, B. H. Pate, *J. Phys. Chem. A* **2004**, *108*, 1365. c) H. S. Yoo, M. J. DeWitt, B. H. Pate, *J. Phys. Chem. A* **2004**, *108*, 1380.

35 A. H. Zewail, *Faraday Discuss. Chem. Soc.* **1983**, *75*, 315.

36 a) P. M. Felker, A. H. Zewail, *J. Chem. Phys.* **1985**, *82*, 2961. b) P. M. Felker, A. H. Zewail, *J. Chem. Phys.* **1985**, *82*, 2975. c) P. M. Felker, A. H. Zewail, *J. Chem. Phys.* **1985**, *82*, 2994.

37 R. Moore, F. E. Doany, E. J. Heilweil, R. M. Hochstrasser, *Faraday Discuss. Chem. Soc.* **1983**, *75*, 331.

38 a) T. Ebata, A. Iwasaki, N. Mikami, *J. Phys. Chem. A* **2000**, *104*, 7974. b) Y. Yamada, J. Okano, N. Mikami, T. Ebata, *J. Chem. Phys.* **2005**, *123*, 124316. c) Y. Yamada, Y. Katsumoto, T. Ebata, *Phys. Chem. Chem. Phys.* **2007**, *9*, 1170.

39 D. J. Nesbitt, R. W. Field, *J. Phys. Chem.* **1996**, *100*, 12735.

40 K. V. Reddy, D. F. Heller, M. J. Berry, *J. Chem. Phys.* **1982**, *76*, 2814.

41 A. Callegari, R. Pearman, S. Choi, P. Engels, H. Srivastava, M. Gruebele, K. K. Lehmann, G. Scoles, *Mol. Phys.* **2003**, *101*, 551.

42 S. Cupp, C. Y. Lee, D. McWhorter, B. H. Pate, *J. Chem. Phys.* **1998**, *109*, 4302.

43 S. Lee, M. Engel, M. Gruebele, *Chem. Phys. Lett.* **2006**, *420*, 151.

44 S. Ishiuchi, H. Shitomi, K. Takazawa, M. Fujii, *Chem. Phys. Lett.* **1998**, *283*, 243.

45 M. Quack, J. Stohner, *J. Phys. Chem.* **1993**, *97*, 12574.

46 A. A. Stuchebrukhov, A. Mehta, R. A. Marcus, *J. Phys. Chem.* **1993**, *97*, 12491.

47 W. Dietz, F. Fischer, *J. Chem. Phys.* **2000**, *113*, 2741.

48 R. Rey, J. T. Hynes, *J. Chem. Phys.* **1996**, *104*, 2356.

49 a) J. Yarwood, R. Ackroyd, G. N. Robertson, *Chem. Phys. Lett.* **1981**, *78*, 614. b) U. P. Agarwal, R. S. Green, J. Yarwood, *Chem. Phys.* **1983**, *74*, 35.

50 H. Abramczyk, W. Reimschüssel, H. Barańska, A. Labudzińska, *Chem. Phys.* **1985**, *94*, 435.

51 R. Laenen, C. Rauscher, J. Simeonidis, *J. Chem. Phys.* **1999**, *110*, 5814.

52 D. D. Dlott, *Chem. Phys.* **2001**, *266*, 149.

53 J. Zheng, K. Kwak, J. Asbury, X. Chen, I. R. Piletic, M. J. Fayer, *Science* **2005**, *309*, 1338.

54 M. L. Cowan, B. D. Bruner, N. Huse, J. R. Dwyer, B. Chugh, E. T. J. Nibbering, T. Elsaesser, R. J. D. Miller, *Nature* **2005**, *434*, 199.

55 P. Schuster, G. Zundel, C. Sandorfy, *The Hydrogen Bond. Recent Developments in Theory and Experiments*, Amsterdam, North-Holland, **1976**, Vol. 2.

56 Y. Yamada, T. Ebata, M. Kayano, N. Mikami, *J. Chem. Phys.* **2004**, *120*, 7400.

57 Y. Yamada, N. Mikami, T. Ebata, *J. Chem. Phys.* **2004**, *121*, 11530.

58 M. Kayano, T. Ebata, Y. Yamada, N. Mikami, *J. Chem.*

Phys. **2004**, *120*, 7410.
59 Y. Yamada, M. Kayano, N. Mikami, T. Ebata, *J. Phys. Chem. A* **2006**, *110*, 6250.
60 Y. Yamada, N. Mikami, T. Ebata, *Proc. Natl. Acad. Sci. U.S.A.* **2008**, *105*, 12690.
61 T. Ebata, Y. Hodono, T. Ito, Y. Inokuchi, *J. Chem. Phys.* **2007**, *126*, 141101.
62 a) R. Kusaka, Y. Inokuchi, T. Ebata, *Phys. Chem. Chem. Phys.* **2007**, *9*, 4452. b) R. Kusaka, Y. Inokuchi, T. Ebata, *Phys. Chem. Chem. Phys.* **2008**, *10*, 6238.
63 C. D. Gutsche, *Calixarenes* in *Monographss in Supramolucular Chemistry*, ed. by J. F. Stoddart, Royal Society of Chemistry, Cambridge, **1989**.
64 D. J. Cram, J. M. Cram, *Container Molecules and Their Guests* in *Monographss in Supramolucular Chemistry*, ed. by J. F. Stoddart, Royal Society of Chemistry, **1994**.
65 C. D. Gutsche, *Calixarenes Revisited* in *Monographss in Supramolucular Chemistry*, ed. by J. F. Stoddart, Royal Society of Chemistry, Cambridge, **1998**.
66 C. J. Pedersen, *Science* **1988**, *241*, 536.
67 F. Benevelli, W. Kolodziejski, K. Wozniak, J. Klinowski, *Chem. Phys. Lett.* **1999**, *308*, 65.
68 M. A. Molins, P. M. Nieto, C. Sanchez, P. Prados, J. De Mendoza, M. Pons, *J. Org. Chem.* **1992**, *57*, 6924.
69 S. Buscemi, A. Pace, A. P. Piccionello, S. Pappalardo, D. Garozzo, T. Pilati, G. Gattuso, A. Pappalardo, I. Pisagatti, M. F. Parisi, *Tetrahedron Lett.* **2006**, *47*, 9049.
70 R. Kuzmicz, L. Dobrzycki, K. Wozniak, F. Benevelli, J. Klinowski, W. Kolodziejski, *Phys. Chem. Chem. Phys.* **2002**, *4*, 2387.
71 Y. V. Fedorov, O. Fedorova, N. Schepel, M. Alfimov, A. M. Turek, J. Saltiel, *J. Phys. Chem. A* **2005**, *109*, 8653.
72 G. W. Buchanan, M. F. Rastegar, *Solid State Nucl. Magn. Reson.* **2001**, *20*, 137.
73 A. S. Denisova, E. M. Dem'yanchuk, G. L. Starova, L. A. Myund, A. A. Makarov, A. A. Simanova, *J. Mol. Struct.* **2007**, *828*, 1.
74 C. Endicott, H. L. Strauss, *J. Phys. Chem. A* **2007**, *111*, 1236.
75 K. Fukuhara, M. Tachikake, S. Matsumoto, H. Matsuura, *J. Phys. Chem.* **1995**, *99*, 8617.
76 C. A. Schalley, R. K. Castellano, M. S. Brody, D. M. Rudkevich, G. Siuzdak, J. Rebek, Jr., *J. Am. Chem. Soc.* **1999**, *121*, 4568.
77 R. Zadmard, A. Kraft, T. Schrader, U. Linne, *Chem.—Eur. J.* **2004**, *10*, 4233.
78 S. Ishikawa, T. Ebata, N. Mikami, *J. Chem. Phys.* **1999**, *110*, 9504.
79 R. Yamamoto, S. Ishikawa, T. Ebata, N. Mikami, *J. Raman Spec.* **2000**, *31*, 295.
80 R. Yamamoto, T. Ebata, N. Mikami, *J. Chem. Phys.* **2001**, *114*, 7866.
81 R. Yamamoto, T. Ebata, N. Mikami, *Eur. Phys. J. D* **2002**, *20*, 403.
82 M. J. Frisch, G. W. Trucks, H. B. Schlegel, G. E. Scuseria, M. A. Robb, J. R. Cheeseman, J. A. Montgomery, Jr., T. Vreven, K. N. Kudin, J. C. Burant, J. M. Millam, S. S. Iyengar, J. Tomasi, V. Barone, B. Mennucci, M. Cossi, G. Scalmani, N. Rega, G. A. Petersson, H. Nakatsuji, M. Hada, M. Ehara, K. Toyota, R. Fukuda, J. Hasegawa, M. Ishida, T. Nakajima, Y. Honda, O. Kitao, H. Nakai, M. Klene, X. Li, J. E. Knox, H. P. Hratchian, J. B. Cross, C. Adamo, J. Jaramillo, R. Gomperts, R. E. Stratmann, O. Yazyev, A. J. Austin, R. Cammi, C. Pomelli, J. W. Ochterski, P. Y. Ayala, K. Morokuma, G. A. Voth, P. Salvador, J. J. Dannenberg, V. G. Zakrzewski, S. Dapprich, A. D. Daniels, M. C. Strain, O. Farkas, D. K. Malick, A. D. Rabuck, K. Raghavachari, J. B. Foresman, J. V. Ortiz, Q. Cui, A. G. Baboul, S. Clifford, J. Cioslowski, B. B. Stefanov, G. Liu, A. Liashenko, P. Piskorz, I. Komaromi, R. L. Martin, D. J. Fox, T. Keith, M. A. Al-Laham, C. Y. Peng, A. Nanayakkara, M. Challacombe, P. M. W. Gill, B. Johnson, W. Chen, M. W. Wong, C. Gonzalez, J. A. Pople, *Gaussian 03, Revision B.05*, Gaussian, Inc., Pittsburgh PA, **2003**.
83 *CRC Handbook of Chemistry and Physics*, 76th ed., CRC Press Boca Raton, New York, London, Tokyo, **1995–1996**.
84 T. Kobayashi, K. Honma, O. Kajimoto, S. Tsuchiya, *J. Chem. Phys.* **1987**, *86*, 1111.
85 T. Kobayashi, O. Kajimoto, *J. Chem. Phys.* **1987**, *86*, 1118.
86 T. Kobayashi, O. Kajimoto, *Res. Chem. Intermed.* **1998**, *24*, 785.
87 R. M. Helm, H.-P. Vogel, H. J. Neusser, V. Storm, D. Consalvo, H. Dreizler, *Z. Naturforsch.* **1997**, *52a*, 655.
88 Y. Matsumoto, T. Ebata, N. Mikami, *J. Chem. Phys.* **1998**, *109*, 6303.
89 L. C. Snoek, E. G. Robertson, R. T. Kroemer, J. P. Simons, *Chem. Phys. Lett.* **2000**, *321*, 49.
90 E. G. Robertson, J. P. Simons, *Phys. Chem. Chem. Phys.* **2001**, *3*, 1.
91 G. von Helden, I. Compagnon, M. N. Blom, M. Frankowski, U. Erlekam, J. Oomens, B. Brauer, R. B. Gerber, G. Meijer, *Phys. Chem. Chem. Phys.* **2008**, *10*, 1248.
92 K. T. Lee, J. Sung, K. J. Lee, S. K. Kim, Y. D. Park, *J. Chem. Phys.* **2002**, *116*, 8251.
93 J. R. Carney, B. C. Dian, G. M. Florio, T. S. Zwier, *J. Am. Chem. Soc.* **2001**, *123*, 5596.
94 M. Schmidt, M. Mons, J. Le Calvé, *Chem. Phys. Lett.* **1991**, *177*, 371.
95 M. Mons, J. Le Calvé, F. Piuzzi, I. Dimicoli, *J. Chem. Phys.* **1990**, *92*, 2155.
96 J. E. Wessel, J. A. Syage, *J. Phys. Chem.* **1990**, *94*, 737.
97 A. Müller, F. Talbot, S. Leutwyler, *J. Chem. Phys.* **2002**, *116*, 2836.
98 J. T. Yi, J. W. Ribblett, D. W. Pratt, *J. Phys. Chem. A* **2005**, *109*, 9456.
99 Z. S. Huang, R. E. Miller, *J. Chem. Phys.* **1989**, *91*, 6613.
100 T. Watanabe, N. Mikami, T. Ebata, unpublished results.
101 M. Bixon, J. Jortner, *J. Chem. Phys.* **1968**, *48*, 715.
102 D. F. Heller, S. Mukamel, *J. Chem. Phys.* **1979**, *70*, 463.
103 J. S. Hutchinson, W. P. Reinhardt, J. T. Hynes, *J. Chem. Phys.* **1983**, *79*, 4247.
104 A. McIlroy, D. J. Nesbitt, *J. Chem. Phys.* **1990**, *92*, 2229.
105 A. A. Stuchebrukhov, R. A. Marcus, *J. Chem. Phys.* **1993**, *98*, 6044.
106 M. Quack, *Faraday Discuss. Chem. Soc.* **1983**, *75*, 359.
107 T. Ebata, A. Iwasaki, N. Mikami, *J. Phys. Chem. A* **2000**, *104*, 7974.
108 F. Lahmani, A. Tramer, C. Tric, *J. Chem. Phys.* **1974**, *60*, 4431.
109 C. Tric, *Chem. Phys. Lett.* **1973**, *21*, 83.
110 P. M. Felker, A. H. Zewail, *Phys. Rev. Lett.* **1984**, *53*, 501.
111 D. Goswami, W. S. Warren, *J. Chem. Phys.* **1993**, *99*, 4509.
112 Y. Yamada, Ph.D. Thesis, Tohoku University, Sendai, **2006**.
113 J. T. Yardly, *Introduction to Molecular Energy Transfer*, Academic, New York, **1980**.

Takayuki Ebata received his Ph.D. degree from Tokyo Institute of Technology in 1981 under the direction of Prof. Ikuzo Tanaka. He was appointed as a research associate in the Department of Chemistry at Tohoku University in 1981, and promoted as an associate professor in 1993. From 1984 to 1986, he did postdoctoral research at Stanford University in the group of Prof. Richard Zare. His awards include a subsidy from Morino foundation (1990), Takaoka citizen's award (1997), and award for scientific measurements (1998). He has devoted himself to the development of nonlinear laser spectroscopy of gas-phase molecules and clusters under jet-cooled conditions.